

SERDP SEED PROJECT UX-1287 FINAL REPORT

IMPROVING UXO/CLUTTER DISCRIMINATION PERFORMANCE THROUGH ADAPTIVE PROCESSING

June 2003

PERFORMING ORGANIZATIONS

**AETC Incorporated
1225 Jefferson Davis Hwy.
Suite 800
Arlington, VA 22202**

**Duke University
Pratt School of Engineering
Dept. of Electrical Engineering & Computer Engineering
Box 90291
Durham, NC 27708**

This research was supported wholly by the U.S. Department of Defense, through the Strategic Environmental Research and Development Program (SERDP) through SEED Project UX-1287 under Contract DACA72-02-P-0048.

VIEWS, OPINIONS, AND/OR FINDINGS CONTAINED IN THIS REPORT ARE THOSE OF THE AUTHOR(S) AND SHOULD NOT BE CONSTRUED AS AN OFFICIAL DEPARTMENT OF THE ARMY POSITION, POLICY, OR DECISION, UNLESS SO DESIGNATED BY OTHER OFFICIAL DOCUMENTATION.

Report Documentation Page				Form Approved OMB No. 0704-0188	
Public reporting burden for the collection of information is estimated to average 1 hour per response, including the time for reviewing instructions, searching existing data sources, gathering and maintaining the data needed, and completing and reviewing the collection of information. Send comments regarding this burden estimate or any other aspect of this collection of information, including suggestions for reducing this burden, to Washington Headquarters Services, Directorate for Information Operations and Reports, 1215 Jefferson Davis Highway, Suite 1204, Arlington VA 22202-4302. Respondents should be aware that notwithstanding any other provision of law, no person shall be subject to a penalty for failing to comply with a collection of information if it does not display a currently valid OMB control number.					
1. REPORT DATE JUN 2003		2. REPORT TYPE		3. DATES COVERED 00-00-2003 to 00-00-2003	
4. TITLE AND SUBTITLE Improving UXO/Clutter Discrimination Performance Through Adaptive Processing				5a. CONTRACT NUMBER	
				5b. GRANT NUMBER	
				5c. PROGRAM ELEMENT NUMBER	
6. AUTHOR(S)				5d. PROJECT NUMBER	
				5e. TASK NUMBER	
				5f. WORK UNIT NUMBER	
7. PERFORMING ORGANIZATION NAME(S) AND ADDRESS(ES) AETC Incorporated,1225 Jefferson Davis Hwy Suite 800,Arlington,VA,22202				8. PERFORMING ORGANIZATION REPORT NUMBER	
9. SPONSORING/MONITORING AGENCY NAME(S) AND ADDRESS(ES)				10. SPONSOR/MONITOR'S ACRONYM(S)	
				11. SPONSOR/MONITOR'S REPORT NUMBER(S)	
12. DISTRIBUTION/AVAILABILITY STATEMENT Approved for public release; distribution unlimited					
13. SUPPLEMENTARY NOTES					
14. ABSTRACT Many cart- and vehicular-based unexploded ordnance (UXO) detection systems employ global positioning system (GPS) receivers to accurately determine the system's position. However, the unevenness of the terrain often causes the system to tilt during the data collection, introducing errors in the GPS measurements. In this work, three approaches are considered to correct the errors in the GPS measurements caused by the tilting of the system: low-pass filtering (LPF) linear predictive filtering, and adaptive filtering using a hidden Markov model (HMM). The LPF smooths the data collection path recorded by the GPS receiver. Although this filter does not explicitly model the system motion, it does remove dramatic, and unrealistic, jumps in the GPS measurements. In contrast, the movement of the system can be explicitly modeled by an HMM. The HMM characterizes the cart motion so that the subsequent filtering is appropriate for the type of motion encountered. The error correction techniques are first applied to simulated data in which both the sources of error and the ground truth are known so that the performance of the algorithms can be compared. The algorithms are then applied to measured data collected with a cart-based system to evaluate the robustness of their performance. Although the HMM approach is found to represent an improvement over the LPF, robustness issues remain with this approach ? mainly through ambiguities in the cart orientation. A quaternion formulation is therefore proposed as a possible efficient means to track and process the cart orientation as it moves over the uneven terrain.					
15. SUBJECT TERMS					
16. SECURITY CLASSIFICATION OF:			17. LIMITATION OF ABSTRACT Same as Report (SAR)	18. NUMBER OF PAGES 59	19a. NAME OF RESPONSIBLE PERSON
a. REPORT unclassified	b. ABSTRACT unclassified	c. THIS PAGE unclassified			

Abstract

Many cart- and vehicular-based unexploded ordnance (UXO) detection systems employ global positioning system (GPS) receivers to accurately determine the system's position. However, the unevenness of the terrain often causes the system to tilt during the data collection, introducing errors in the GPS measurements. In this work, three approaches are considered to correct the errors in the GPS measurements caused by the tilting of the system: low-pass filtering (LPF), linear predictive filtering, and adaptive filtering using a hidden Markov model (HMM). The LPF smooths the data collection path recorded by the GPS receiver. Although this filter does not explicitly model the system motion, it does remove dramatic, and unrealistic, jumps in the GPS measurements. In contrast, the movement of the system can be explicitly modeled by an HMM. The HMM characterizes the cart motion so that the subsequent filtering is appropriate for the type of motion encountered. The error correction techniques are first applied to simulated data, in which both the sources of error and the ground truth are known so that the performance of the algorithms can be compared. The algorithms are then applied to measured data collected with a cart-based system to evaluate the robustness of their performance. Although the HMM approach is found to represent an improvement over the LPF, robustness issues remain with this approach – mainly through ambiguities in the cart orientation. A quaternion formulation is therefore proposed as a possible efficient means to track and process the cart orientation as it moves over the uneven terrain.

Table of Contents

1. Introduction.....	1
2. Models	2
2.1. Cart Path Models	2
2.1.1. Idealized Cart Path Models.....	2
2.1.2. Realistic Cart Path Model	4
2.2. Cart Motion Model	4
2.3. GPS Measurement Error Models.....	6
2.3.1. Uncorrelated Errors	6
2.3.2. Correlated Errors	6
2.4. Sensor Models	8
2.4.1. Electromagnetic Induction.....	8
2.4.2. Magnetometer	8
3. Algorithms	9
3.1. GPS Measurement Filters	9
3.1.1. Low Pass Filters	9
3.1.2. Linear Predictive Filter	10
3.2. Cart Motion Characterization	10
3.3. Sensor Model Parameter Estimation	11
4. Simulation Studies	11
4.1. Sensitivity of Sensor Model Parameter Estimation	11
4.2. Effects of GPS Measurement Error Correlation	13
4.3. Effects of Cart Path Curvature	22
4.4. Impact of Cart Motion Characterization	38
5. Real Data Processing: ATD/JPG	39
6. Three-Dimensional Cart Motion	48
6.1. Quaternions	48
6.2. Advantages of Using Quaternions	51
6.3. A Quaternion Formulation Using GPS Measurements.....	52
7. Summary.....	53
8. Directions for Future Research	54
9. References.....	54
10. Technical Publications.....	55

1. Introduction

The discrimination of unexploded ordnance (UXO) from surrounding metallic clutter poses a great technological challenge. One approach that has shown promise in addressing this challenge makes use of the following important observation: most electromagnetic induction (EMI) signatures of UXO and clutter are very well characterized by a simple induced dipole response model expressed by the eigenvalues of the magnetic polarizability tensor along the object's three principal axes [1-3]. To the extent that these eigenvalues differ between UXO and clutter, discrimination is possible.

Results of inverting controlled EMI measurements, over ordnance and clutter, have demonstrated that a high degree of discrimination is realizable [4-5]. However, when applied to field data – where the sensor positions are generally not precisely known – the same level of success has not been achieved [6]. The reason is simple: because signal amplitude depends strongly on range, positioning errors can cause significant deviations in the signal calculations used in inverting the data. This seriously degrades the ability to capture the subtle spatial variations of the signal that are crucial to discriminating between different types of objects.

The goal of this work is to correct errors in global positioning system (GPS) measurements recorded by a cart-mounted UXO detection system. The UXO detection system includes EMI and magnetometer sensors and a GPS receiver, intended to accurately determine the position of the system, mounted above the cart. Unfortunately, in many instances, the unevenness of the ground causes the system to tilt. When the system tilts, the recorded GPS measurements are offset from the true system positions and discrimination performance is consequently diminished.

The GPS measurement error-correction algorithms presented in this report are intended to reduce the errors in the GPS measurements introduced by the tilting of the cart. Three approaches are considered: low-pass filtering (LPF), linear predictive filtering, and adaptive filtering using a hidden Markov model (HMM). The LPF is the baseline error correction algorithm, and removes dramatic and unrealistic jumps in the GPS measurements even though it does not explicitly model the system motion. The linear predictive filter offers a causal approach, but again does not explicitly model the system motion. The third approach – the HMM approach – does explicitly include the system movement. In this approach, the cart motion is broadly characterized as either linear or nonlinear, after which an appropriate filter is applied.

All three error correction techniques are applied to simulated data – for which both the sources of error and the ground truth are known – so that the performance of the algorithms can be compared. The algorithms are then applied to measured data collected with a cart-based system at the Advanced Technology Demonstration at Jefferson Proving Ground (ATD/JPG) to evaluate their robustness under real conditions.

Finally, in order to address deficiencies in the HMM approach, a quaternion formulation is proposed as a possible means of tracking and processing the cart orientation as it moves over the uneven terrain. The addition of this information is crucial for resolving ambiguities encountered when attempting to characterize the motion as either linear or nonlinear, and offers an opportunity for improved robustness.

The accomplishments include:

- Modeling of cart path, cart motion, GPS measurement errors, and sensors.
- Development of algorithms for GPS measurement error-correction and cart motion characterization.
- Analysis of GPS error correction algorithms through simulation.
- Application of GPS error correction algorithms to data collected at ATD/JPG.
- Modeling of cart orientation using a quaternion formulation.

2. Models

2.1. Cart Path Models

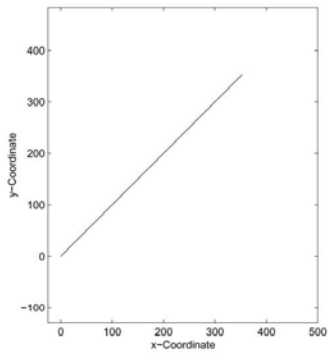
2.1.1. Idealized Cart Path Models

Several idealized cart motion models, which are intended to reveal the effects of curvature of the cart path on algorithm performance, are considered in the simulations. They are shown in Figure 1. For each of the cart paths, the distance between successive cart locations is 1 unit. Since there are 500 measurements in each path, each path covers a distance of 499 units.

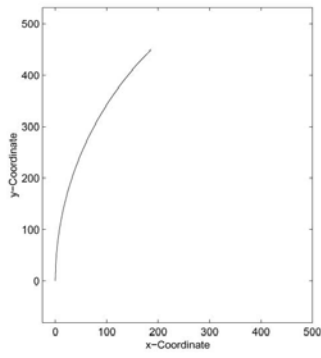
The straight line path and circular paths, shown in subplots (a) through (f), are paths which have a constant curvature over the entire path. The straight line has curvature $\kappa = 0$, and the arcs have curvature $\kappa = \frac{1}{a}$, where a is the radius of the circle. The sinusoidal paths, shown in subplots (g) through (k), have varying curvature over the entire path. For these paths, the curvature is calculated numerically. When the cart path is expressed in vector notation, $\mathbf{P}(t) = x(t)\hat{\mathbf{i}} + y(t)\hat{\mathbf{j}}$, the curvature is

$$\kappa(t) = \frac{|\ddot{x}\dot{y} - \dot{x}\ddot{y}|}{|\dot{\mathbf{v}}|^3},$$

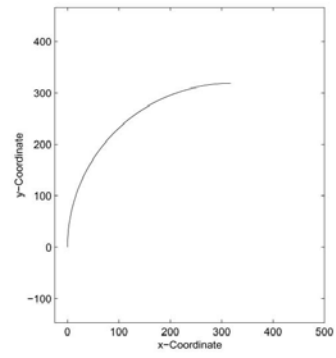
where $\dot{\mathbf{v}}(t) = \dot{\mathbf{P}}(t)$. The curvature of the sinusoidal paths is periodic, with a period twice that of the underlying sinusoidal curve. This is illustrated in Figure 2, which shows the curvature of the path consisting of 3 sinusoid cycles. The simulations presented in Sec. 4.3 show that not only does the curvature of the path affect algorithm performance, but it is also related to the mean RMS error in distance.



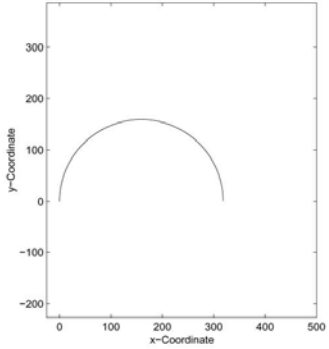
(a) Straight line



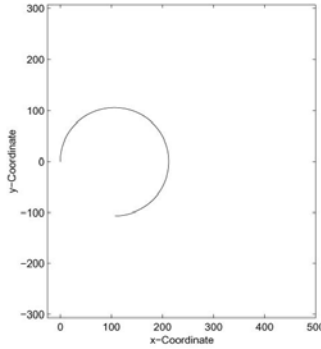
(b) 1/8 Circle



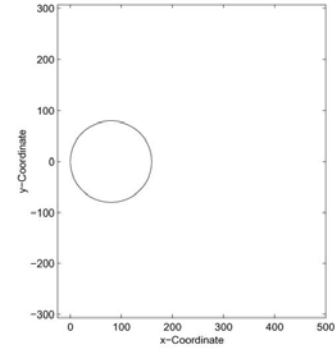
(c) 1/4 Circle



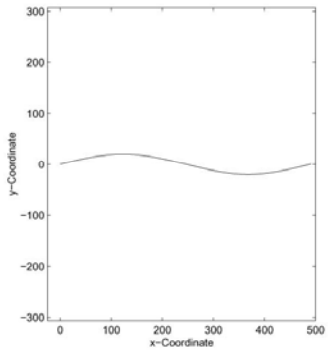
(d) 1/2 Circle



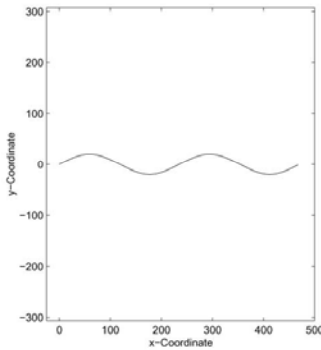
(e) 3/4 Circle



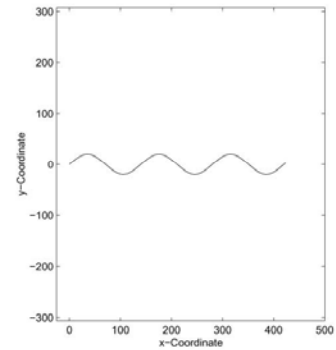
(f) Full Circle



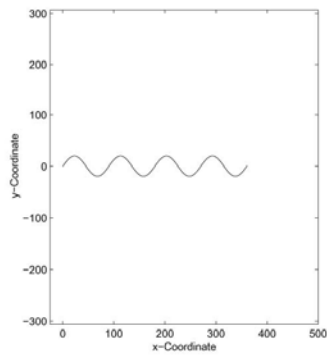
(g) 1 Sinusoid Cycle



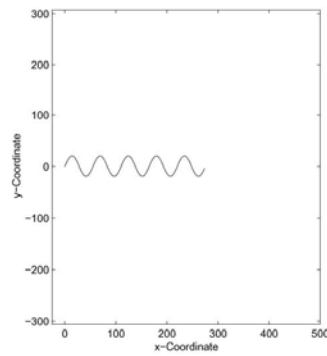
(h) 2 Sinusoid Cycles



(i) 3 Sinusoid Cycles



(j) 4 Sinusoid Cycles



(k) 5 Sinusoid Cycles

Figure 1: Cart paths considered in the simulation studies.

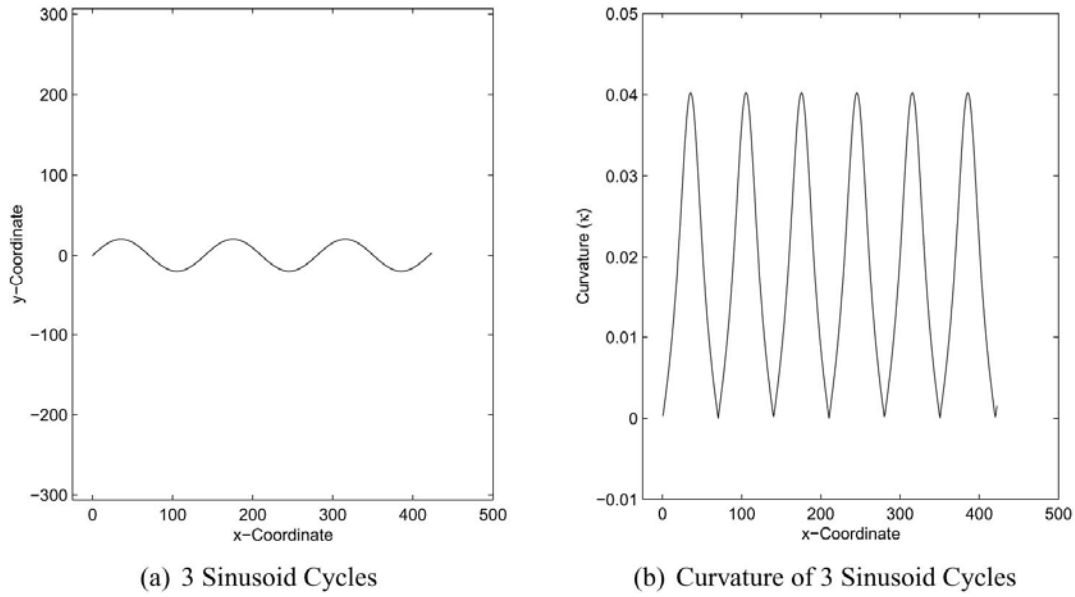


Figure 2: Curvature of the path consisting of 3 Sinusoid Cycles.

2.1.2. Realistic Cart Path Model

A realistic cart path model is depicted in Figure 3. The parameters for the path were chosen to be consistent with the sampling parameters of existing cart and handheld systems. The distance between successive down-track measurements is 5cm, and the distance between adjacent cross-track passes is 0.5m. For the purpose of describing the path, the passes are numbered from bottom to top, so pass 1 is at 0m in the y-direction and pass 6 is at 2.5m in the y-direction. The small bumps in the path, located around $x=1$ m (passes 2-5) and $x=4.2$ m (passes 3-6) in the x-direction, are intended to simulate the perturbations in the GPS measurements induced by tilting of the cart. In addition, detours around obstacles are simulated between 2.5 and 3m in the x-direction in passes 2 and 3, and between 2 and 3m in the x-direction in passes 5 and 6. Finally, the turns between passes are modeled as half-circles.

2.2. Cart Motion Model

The hidden Markov model (HMM) uses the GPS measurements to characterize the cart path as either moving forward, detour to the left, detour to the right, or turn around, and these states are defined for each of the pass directions. The model is depicted in Figure 4. In this model, the observable is the change in the cart position from one measurement to the next. Thus, when the model is in a particular state, that state defines the movement that should occur between the current measurement and the next measurement. For instance, when the model is in the right forward motion state, the next measurement should be 5cm to the right of the current measurement.

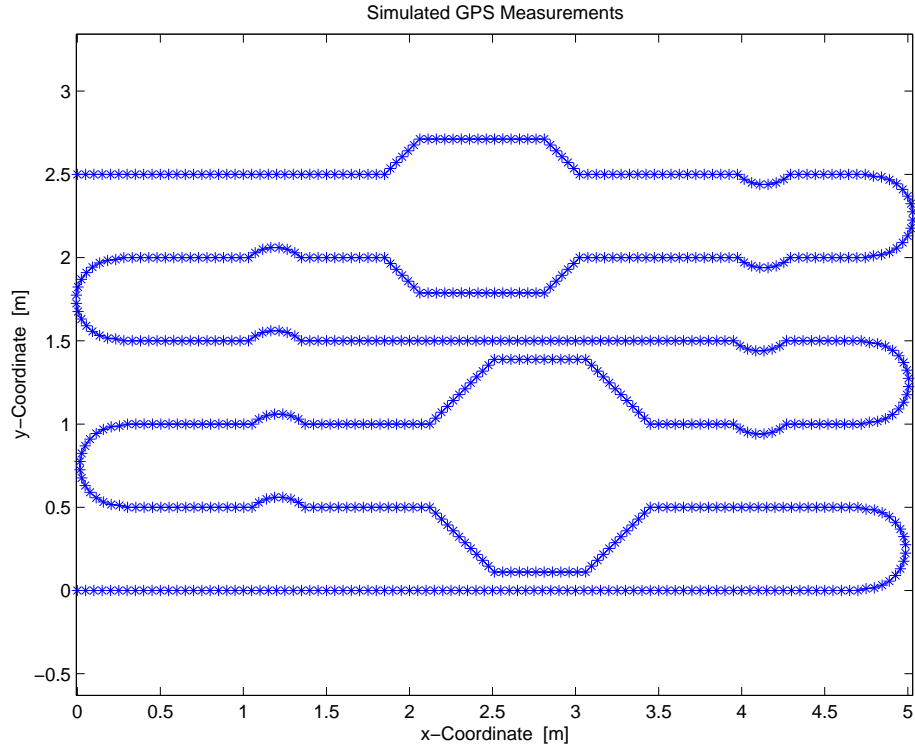


Figure 3: Simulated error-free GPS measurements.

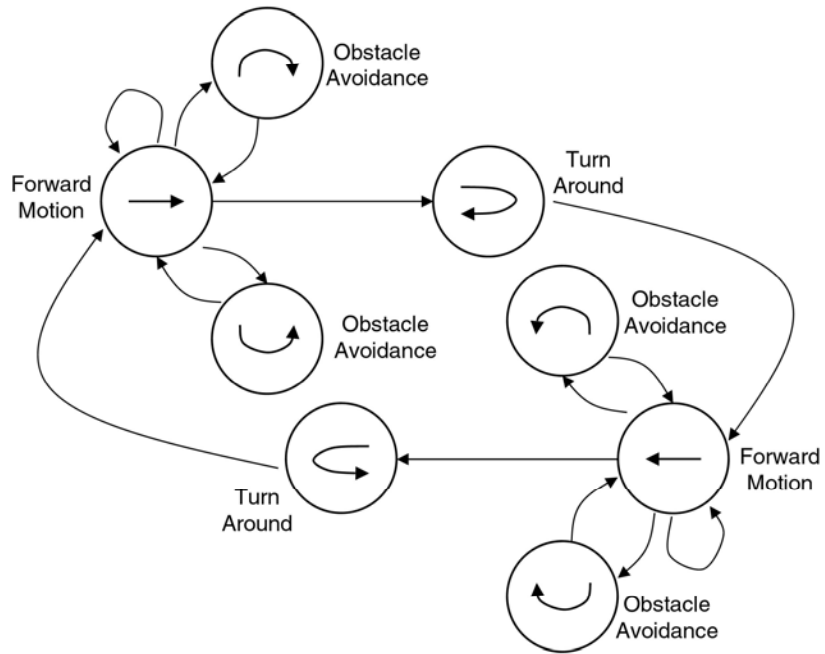


Figure 4: Hidden Markov model for characterizing the cart path.

Each of the detour states is further divided into 5 states. The first two states are the movement away from the ideal straight line path, the third state is movement parallel to the ideal straight line path, and the last two states are movement back toward the ideal straight line path. There are two states moving away from and back toward the ideal path so that detours are forced to be at least 2 measurements away from the ideal path. Using 5 states, rather than 3, eliminated many errors in the estimated state sequence where perturbations in the GPS measurements cause straight line segments to be characterized as small detours. If the characteristics of the detours suggest it would be appropriate, more states can be added to the detour model to force the detour to be farther away from the ideal path. A model in which the detours were characterized by only 3 states was also considered, and the simulations showed that the 5-state detour model was more robust than the 3-state detour model when perturbations in the GPS measurements were caused by cart tilt. Therefore, it is anticipated that forcing the detours to be larger would eliminate more errors in the estimated state sequence where perturbations in the GPS measurements cause straight line segments to be characterized as detours. It is likely that parameters, such as the detour size, will be site dependent.

Each of the turn around states are also divided into several states, and are modeled as known movement in a circular path. For the chosen simulation parameters (5cm between measurements and 0.5m between passes), there are 16 states in each turn around.

2.3. GPS Measurement Error Models

The GPS measurements are modeled as jointly Gaussian. Both uncorrelated and correlated errors are considered, and the effects of correlation in the measurement errors are evaluated through simulations. We believe that assuming a jointly Gaussian model will allow us to work on the error correction algorithms, and also provide the flexibility to determine the model parameters from the actual ground surface and cart dynamics at a later time.

2.3.1. Uncorrelated Errors

Initially, the GPS measurement errors are modeled as uncorrelated jointly Gaussian random variables. An example trajectory (solid line) and the corresponding GPS measurements (open circles) are shown in Figure 5. In this example, the simulated cart path is described by $y=x$, and the GPS measurement errors are uncorrelated Gaussian random variables with variance $\sigma^2 = 0.1$. The degree of error shown here is considered to be moderate for the simulations. The simulations also investigate both larger and smaller error.

2.3.2. Correlated Errors

The GPS measurement error model is extended to include correlation between errors in the x- and y-coordinates. Thus, the model now assumes the measurements in the two coordinate directions are jointly Gaussian with some correlation. The correlated Gaussian random variables were computed by post-multiplying uncorrelated Gaussian random variables by the upper triangular Cholesky decomposition of the desired correlation matrix, R , where

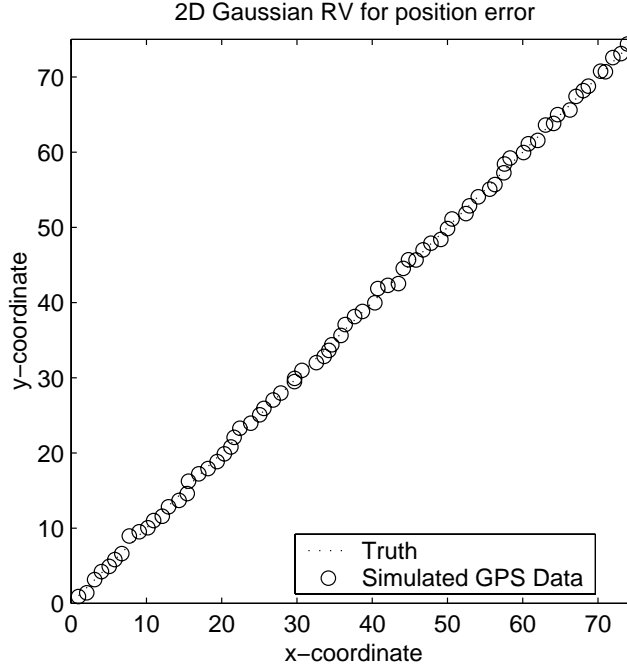


Figure 5: Example cart trajectory (solid line) and corresponding GPS measurements (open circles) for an uncorrelated jointly Gaussian GPS measurement error model.

$$R = \begin{bmatrix} 1 & r \\ r & 1 \end{bmatrix}.$$

In this notation, the cross-correlation between the errors in the x- and y-coordinates is denoted by r .

The effects of correlation in the errors are illustrated in Figure 6. This figure shows an example cart track and the corresponding GPS measurements for uncorrelated ($r = 0$), moderately correlated ($r = 0.5$) and highly correlated ($r = 0.9$) GPS measurement errors for a moderate error level (i.e. variance $\sigma^2 = 0.1$). These examples show that even though the variances of the errors remain constant, the degree of variability appears to be dependent on the correlation. The more correlated the errors are, the less variable they appear to be. The simulations presented in Sec. 4.2 show that the degree of correlation does not affect the performance of the algorithms evaluated in these simulations.

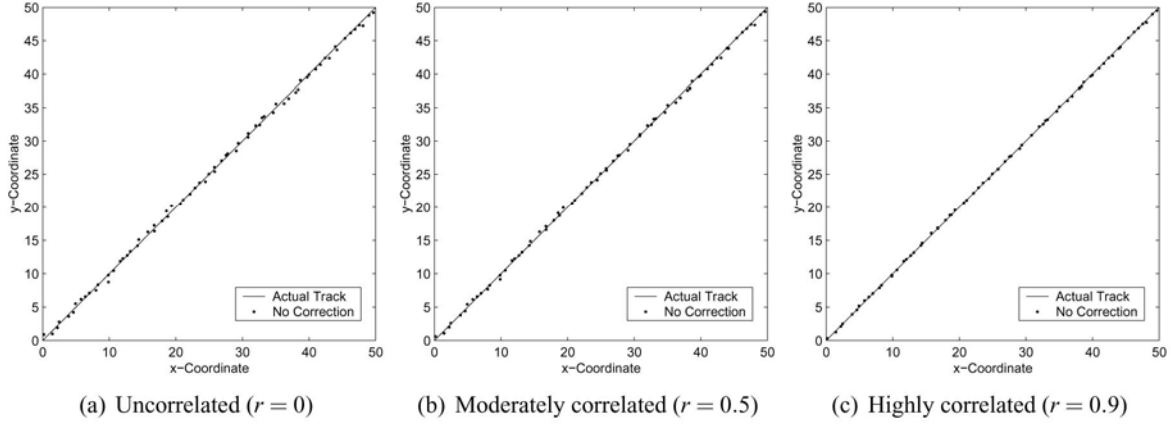


Figure 6: Example cart path (solid line) and corresponding GPS measurements (open circles) for uncorrelated, moderately correlated, and highly correlated GPS measurement errors.

2.4. Sensor Models

The EMI dipole and magnetometer dipole models and parameter estimation algorithms used in these simulations [7] are the same as those used for the vehicular systems, with the appropriate modifications made to make them consistent with the man-portable or handheld system sampling geometries. The model parameters are estimated from measured data, and the resulting estimates utilized for UXO detection and/or discrimination. Thus, it is desirable to have accurate parameter estimates.

2.4.1. Electromagnetic Induction

The EMI dipole model is intended to replicate the EM61 response. There are 5 parameters in the EMI dipole model: the dipole which is composed of the two parameters m_1 and m_2 ($\mathbf{m} = [m_1 \ m_1 \ m_2]$), the target inclination (θ), the target azimuth (ϕ_m), and the target depth (d). The dipole is a function of the physical properties of the target. For UXO, $m_2 > m_1$, and generally $2 \leq \frac{m_2}{m_1} \leq 10$. The target inclination is defined as the angle from the vertical axis (z) through the

target center to the principle axis of the target. Thus, $\theta = 0$ corresponds to a vertical target, and $\theta = \pi/2$ corresponds to a horizontal target. The target azimuth is defined (in the x - y plane) as the angle from the projection of the principle axis of the target to the x -axis. If the cart is traveling parallel to the y -axis, $\phi_m = 0$ describes a target lying perpendicular to the direction of travel, and $\phi_m = \pi/2$ describes a target lying parallel to the direction of travel.

2.4.2. Magnetometer

The magnetometer dipole model has 3 parameters: the target inclination (θ), the target azimuth (ϕ_m), and the target depth (d). The definitions of the target inclination and the target azimuth are the same as for the EMI dipole model.

3. Algorithms

3.1. GPS Measurement Filters

3.1.1. Low Pass Filters

The baseline GPS measurement error correction algorithm is a simple low-pass filter (LPF). Although this approach will reduce large jumps in the GPS measurements, this algorithm does not incorporate models of either the cart motion or the ground surface. Several approaches were taken in designing the LPF. Since a causal filter results in a lag between the actual measurements and the filtered result, only non-causal filters were considered. In addition to a simple moving average filter, other filters which weight the data unequally were also considered. The effects of filter order were evaluated for each of the filters.

The moving average filter is a simple arithmetic average of the $k+1$ (odd) points about the point of interest, where k is the filter order. The impulse response is a rectangular function, and the frequency response is low-pass. Both are shown in Figure 7(a) for a filter order of 6.

The modified moving average filters are similar to the moving average filter, except the tap weights emphasize the points near the point of interest rather than weighting all the points equally. The windowing functions considered were the triangular and Hamming windows. The impulse functions and the corresponding low-pass frequency responses for a filter order of 6 are shown in Figures 7(b) and 7(c), respectively. Both of these filters have a broader frequency response than a rectangular filter of the same length. As expected, the simulation results show that the rectangular filter, which has the narrowest response, has better error-correction performance than either of the other filters.

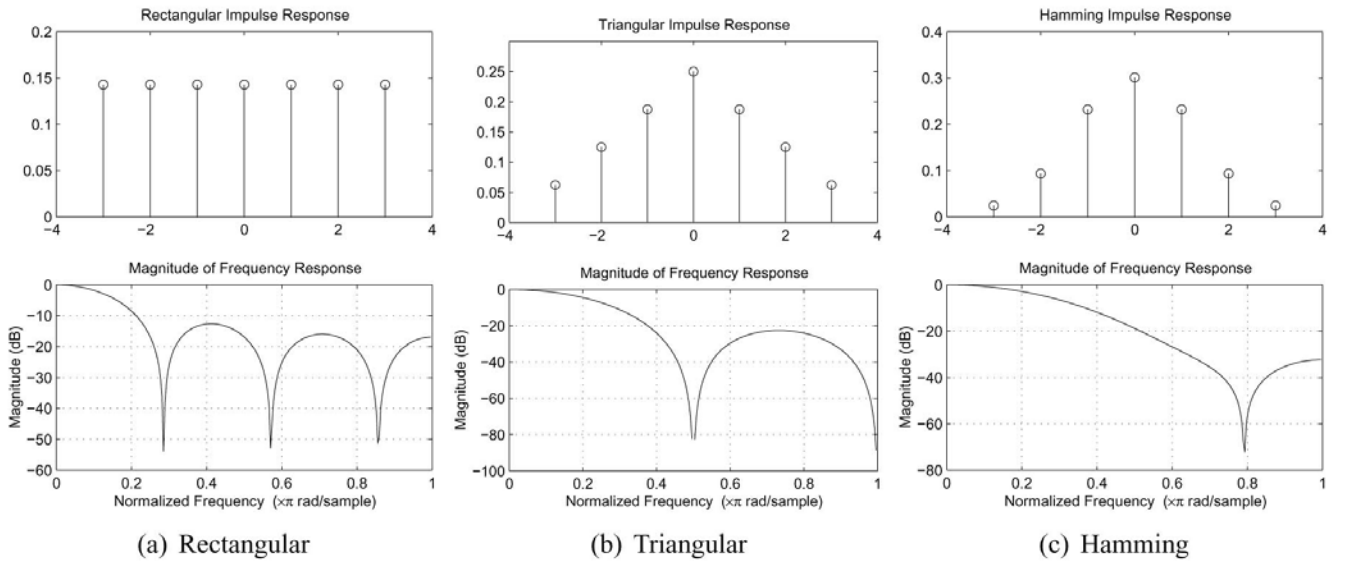


Figure 7: Impulse and frequency responses of the low-pass filters.

3.1.2. Linear Predictive Filter

A linear predictive filter [8] has also been implemented for GPS measurement error correction. Linear prediction differs from the LPF in that it provides a causal solution to error-correcting the GPS measurements. This method assumes a linear model, $z = \alpha m + \beta$, where z is the coordinate of the cart, either x or y , and m is the measurement number.

Linear prediction seeks to minimize the expected value of the squared error between the assumed linear model and the GPS measurement, z_{GPS} , which again is either x_{GPS} or y_{GPS} ,

$$\varepsilon = E[(z_{GPS} - z)^2].$$

Setting the partial derivatives of ε with respect to both α and β equal to zero, yields two equations in two unknowns. The solution to this set of equations, denoted by α_0 and β_0 , is

$$\alpha_0 = \frac{COV[m, z_{GPS}]}{\sigma_m^2} = \frac{\rho \sigma_{z_{GPS}}}{\sigma_m}$$

and

$$\beta_0 = \overline{z_{GPS}} - \alpha_0 \overline{m}.$$

Thus, the parameters for the linear model, α_0 and β_0 , are determined from the data, and the estimate of the current coordinate is calculated from the model by $\hat{z} = \alpha_0 m + \beta_0$.

As applied to this problem, the linear predictive filter of order k uses the previous k GPS measurements as well as the current measurement, for a total of $k + 1$ points, to estimate the current coordinate.

3.2. Cart Motion Characterization

The cart motion state sequence – from which the cart motion is characterized as linear or nonlinear – is estimated using the Viterbi algorithm [9]. The Viterbi algorithm is a useful method for finding the maximum *a posteriori* (MAP) estimate of the state sequence of a finite-state discrete-time Markov process observed in memory-less noise when the output of the process is a function of its current state. It accomplishes this by finding the state sequence which maximizes the conditional *a posteriori* probability of the state sequence given the noisy observations.

For a system with S states and O observations, the number of possible states sequences is S^O . Thus, the computational intensity grows exponentially with the number of observations if the conditional *a posteriori* probability is calculated for every possible state sequence. However, the Viterbi algorithm reduces the computational intensity to linear growth by determining the most likely state sequence leading to every possible ending state after each observation. In this way, after every observation the number of remaining state sequences is equal to the number of

possible ending states, and the search space for the next observation is greatly reduced. This remains an optimal solution to the maximization problem because the most likely state sequence leading to any state after observation o must include one of the most likely state sequences determined after observation $o-1$. Thus, the Viterbi algorithm naturally lends itself to a sequential implementation.

3.3. Sensor Model Parameter Estimation

The sensor model parameters are estimated from measured data, and the resulting estimates used for UXO detection and/or discrimination. For the simulations investigating the effects of GPS positional errors on model parameter estimation, noise-free data is first simulated on a perfect grid, simulating the sampling intervals of the handheld system. In all the simulations, the data is generated assuming that a pass is made directly over the center of the target. After the simulated data is computed, the coordinates of the grid are perturbed to simulate GPS measurement errors. The parameters for the sensor model are then estimated from the simulated sensor data and the perturbed coordinates.

The parameter inversion process is illustrated in Figure 8 using EMI sensor data. For this example, the EMI dipole model parameters are $\mathbf{m} = [10 \ 10 \ 20]$, $\theta = \pi/2$, $\phi_m = \pi/2$, and $d = 0.75\text{m}$. The measurements are taken at 0.05m intervals in the down-track direction and 0.5m intervals in the cross-track direction. The data is displayed with the original sample locations (denoted by 'x') and the perturbed sample locations (denoted by 'o') superimposed in subplots (a) and (b), respectively, for a moderate error level ($\sigma^2 = 10^{-4} \text{ m}^2$ in total distance). The data, which is assumed to have been measured at the irregularly spaced points shown in subplot (b), is then interpolated to a perfect grid, as shown in subplot (c). The dipole parameters are estimated from the interpolated data, and simulated data generated using the parameter estimates is shown in subplot (d). In this example, the estimated EMI dipole model parameters are $\mathbf{m} = [10.0511 \ 10.0511 \ 20.0966]$, $\theta = 0.4996\pi$, $\phi_m = 0.5005\pi$, and $d = 0.7513\text{m}$.

4. Simulation Studies

4.1. Sensitivity of Sensor Model Parameter Estimation

The sensitivity of the EMI and magnetometer dipole models to perturbations in the GPS measurements is evaluated through simulations. The simulations are performed for a variety of dipole model parameters, which are listed in Table 1. All 5 parameters apply to the EMI simulations; however, only θ , ϕ_m , and d apply to the magnetometer simulations. Therefore, only simulations 1 through 4 are performed for the magnetometer model.

The RMS errors are computed from 100 independent realizations of GPS measurement errors. The variance of the GPS measurement errors, as measured by total distance, ranges from 10^{-6} to 10^{-3} m^2 . The corresponding variances in the x- and y-coordinates are $10^{-6}/\sqrt{2}$ to $10^{-3}/\sqrt{2} \text{ m}^2$. The dipole model parameters are estimated from each realization 10 times, with the initial conditions selected randomly for each estimation in order to avoid the problem of convergence at a local minimum, rather than a global minimum. The estimated parameters for each realization are selected by choosing the estimation results which result in the lowest error. In all the

simulations, the simulated sensor data is noise-free. In addition, the realizations which fail to converge at the global minimum are removed from the data before the RMS errors are computed. In all cases, at least 98 realizations are retained to calculate the RMS error.

Simulation	m_1	m_2	θ	ϕ_m	d
1	10	20	0.5π	0.5π	0.75m
2	10	50	0	0	0.75m
3	10	50	0	0.5π	0.75m
4	10	50	0.5π	0	0.75m
5	10	50	0.5π	0.5π	0.75m
6	10	100	0.5π	0.5π	0.75m

Table 1: EMI and magnetometer dipole model simulation parameters.

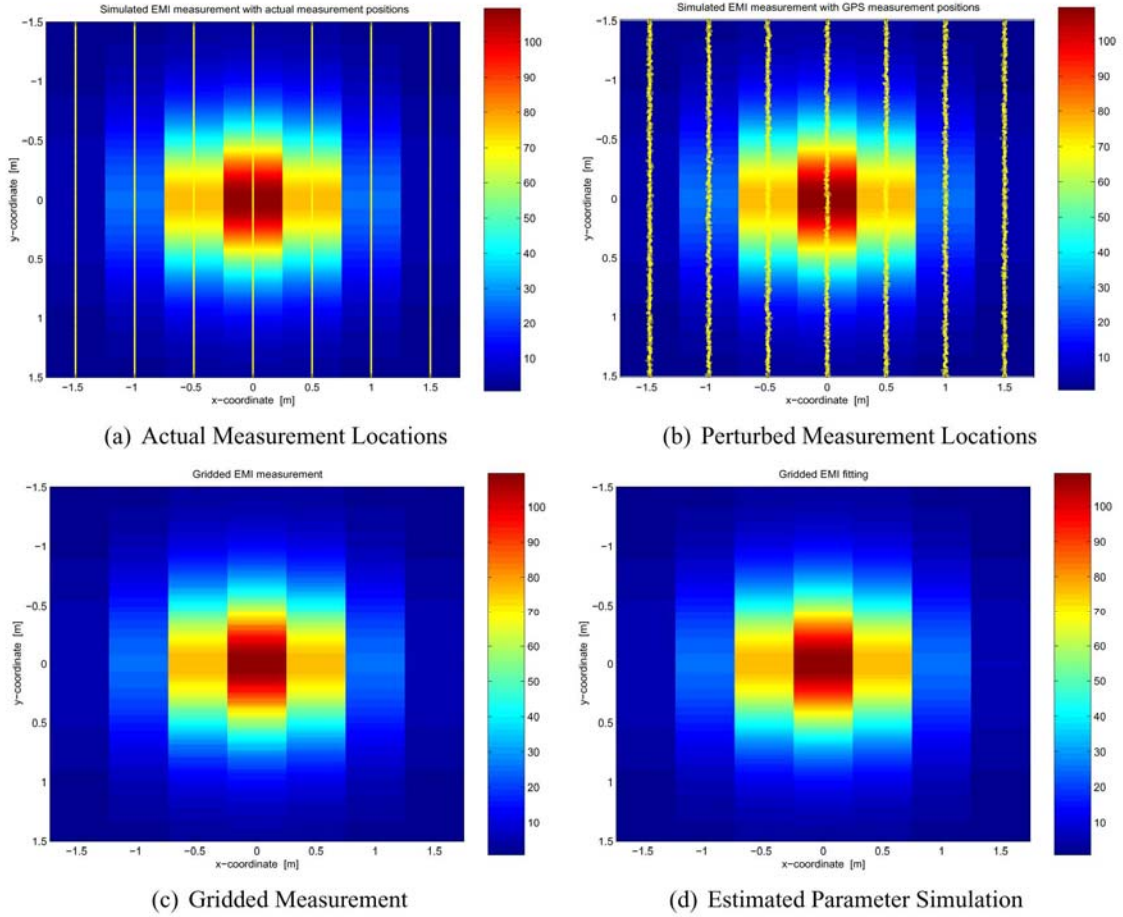
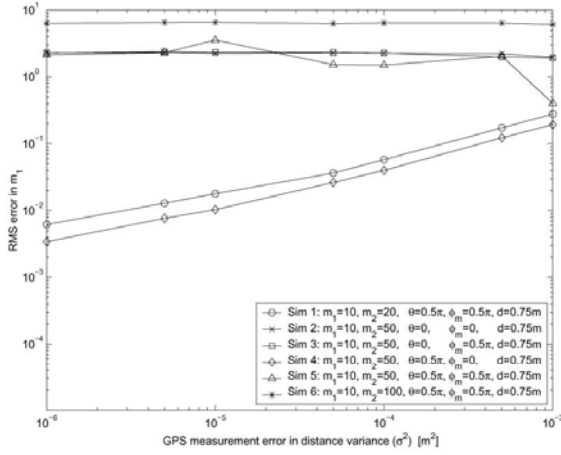


Figure 8: Example EMI dipole model parameter estimation with perturbed GPS measurements. The actual model parameters are $m_1 = 10$, $m_2 = 20$, $\theta = 0.5\pi$, $\phi_m = 0.5\pi$, and $d = 0.75\text{m}$, and the estimated model parameters are $m_1 = 10.0511$, $m_2 = 20.0966$, $\theta = 0.4996\pi$, $\phi_m = 0.5005\pi$, and $d = 0.7513\text{m}$.

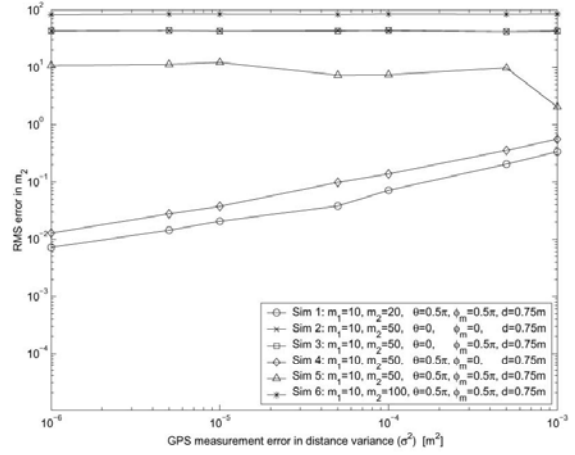
Figures 9 and 10 show the RMS errors in the EMI and magnetometer parameter estimates as a function of the GPS measurement error variance, measured in distance, for each of the simulations. As expected, the results show that decreasing the variance in the GPS measurement errors tends to reduce the RMS error in the dipole model parameter estimates. As this set of simulations illustrates, the improvement in the parameter estimates depends on both the target dipole parameters and the orientation of the target relative to the data collection. For example, the RMS error in the estimate of ϕ_m (target azimuth) is independent of the GPS measurement error variance for simulations 2, 3, and 6, and decreases with the GPS measurement error variance for simulations 1, 4, and 5.

4.2. Effects of GPS Measurement Error Correlation

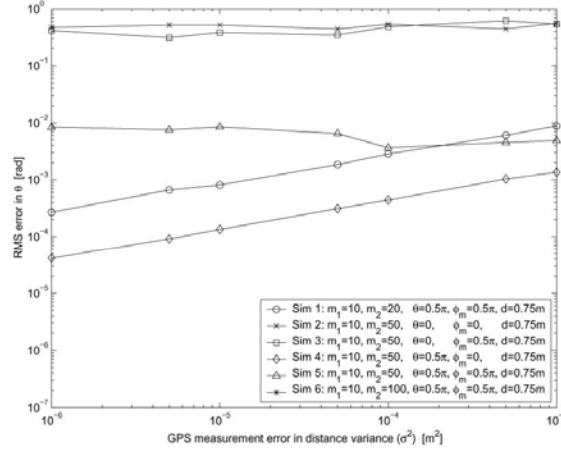
The effects of correlation in the measurement errors are investigated through simulations for the straight line and half circle cart paths at all three error levels. The mean RMS errors as a function of filter order for both the x- and y-coordinates as well as overall distance are shown in Figures 11 through 16. The results in these figures show that for the algorithms considered here, the mean RMS error is not a function of the measurement error correlation. This result is not surprising since the current algorithms operate on the x- and y-coordinate data separately. It is anticipated that the correlation will affect the performance of future algorithms which operate on the two coordinates simultaneously. It is interesting to note that the half circle cart path results show that higher filter order does not necessarily provide better performance. This is due to the curvature of the cart path, which is discussed in the following section.



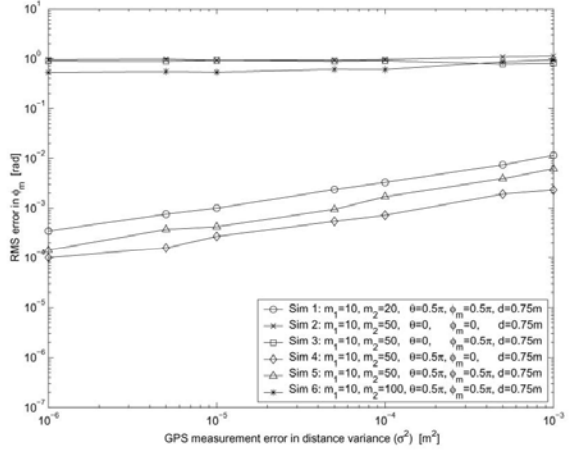
(a) RMS error in m_1



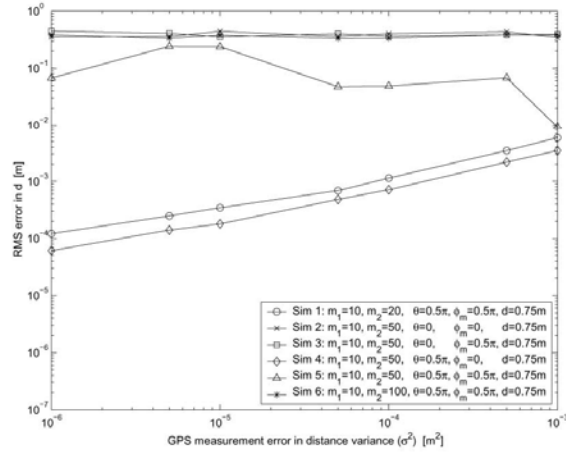
(b) RMS error in m_2



(c) RMS error in θ

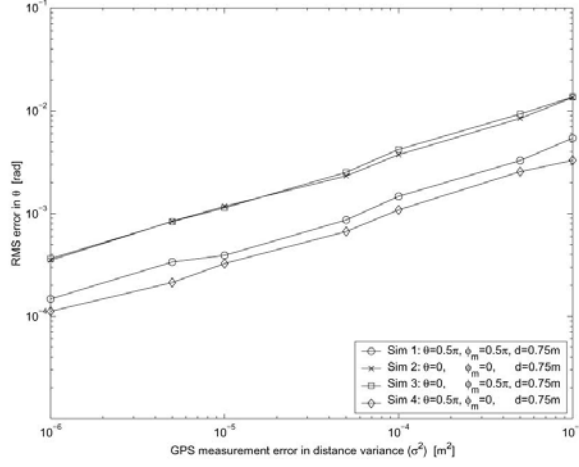


(d) RMS error in ϕ_m

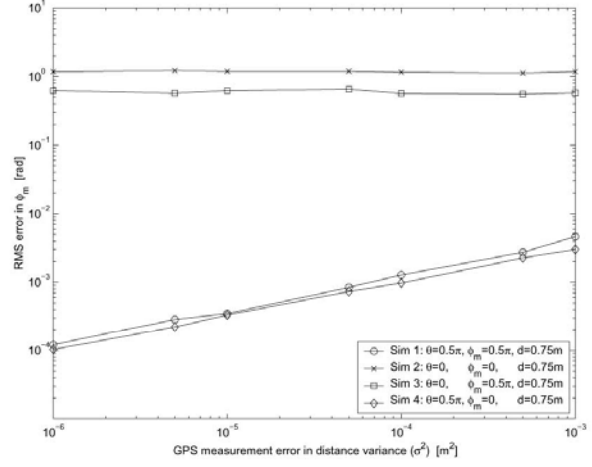


(e) RMS error in d

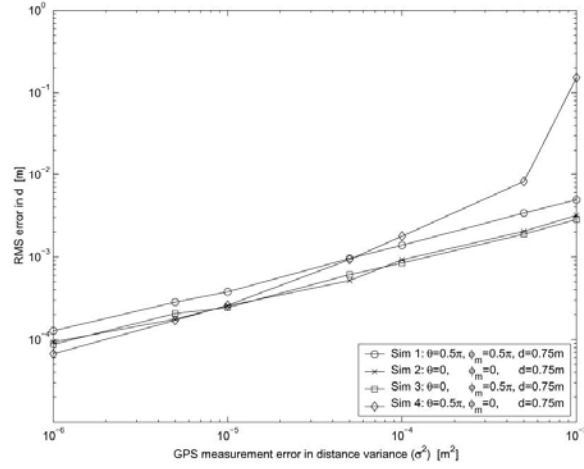
Figure 9: RMS errors in the EMI dipole model parameter estimates as a function of the GPS



(a) RMS error in θ

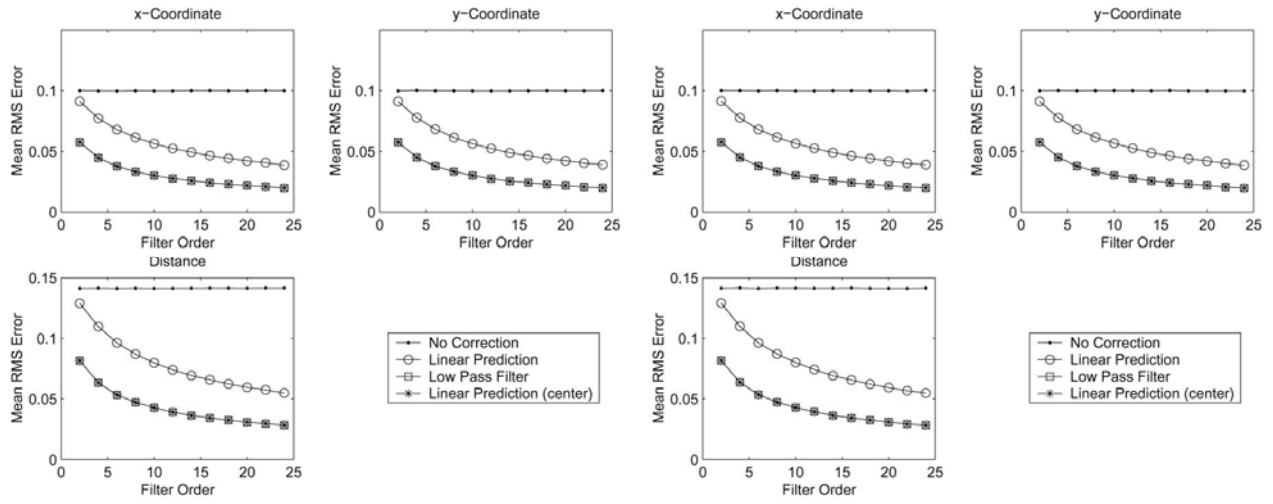


(b) RMS error in ϕ_m



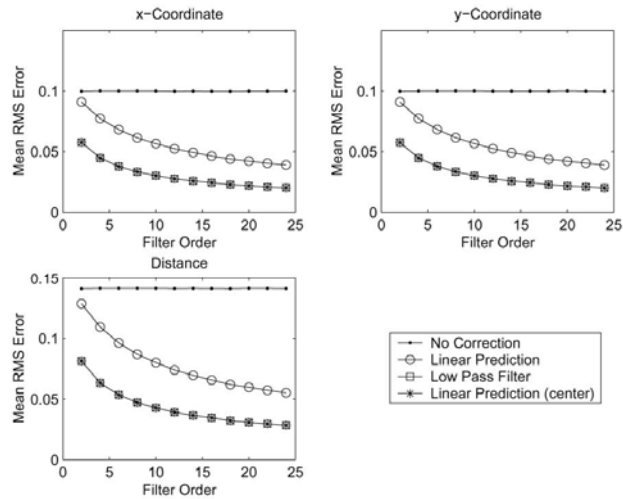
(c) RMS error in d

Figure 10: RMS errors in the magnetometer dipole model parameter estimates as a function of the GPS measurement error variance (measured in distance) for all the simulations.



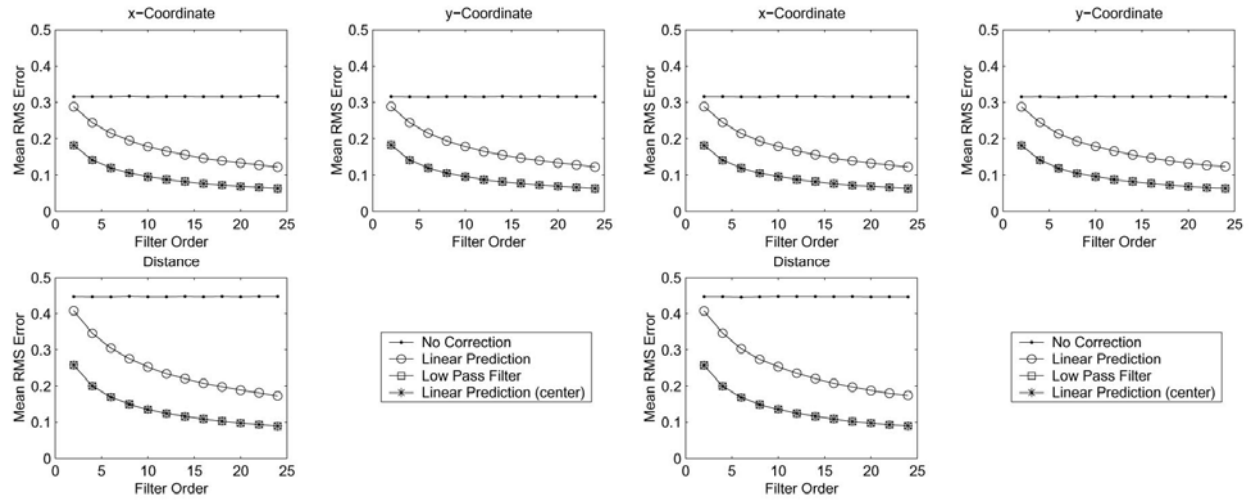
(a) Uncorrelated ($r = 0$)

(b) Moderately correlated ($r = 0.5$)



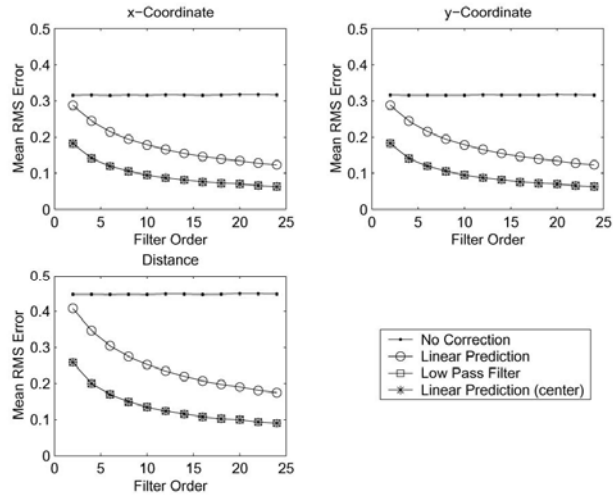
(c) Highly correlated ($r = 0.9$)

Figure 11: RMS Error as a function of filter order for the straight line cart path with low measurement error ($\sigma^2 = 0.01$).



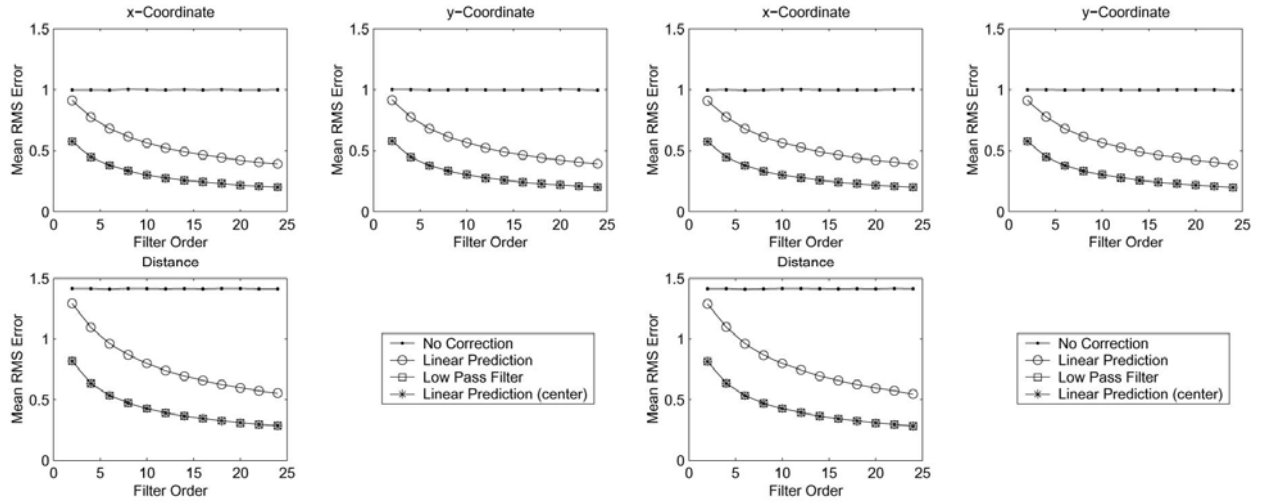
(a) Uncorrelated ($r = 0$)

(b) Moderately correlated ($r = 0.5$)



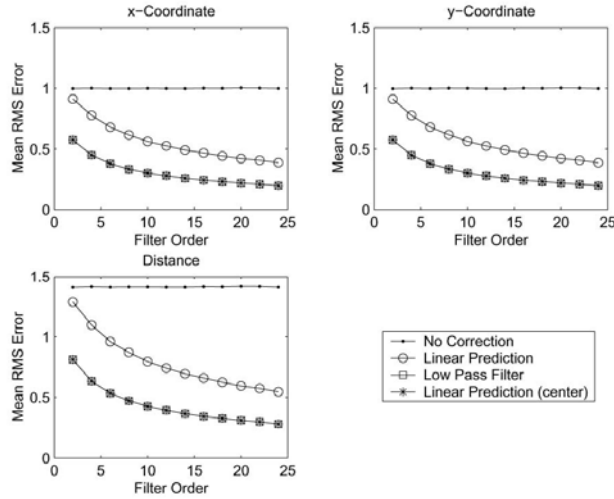
(c) Highly correlated ($r = 0.9$)

Figure 12: RMS Error as a function of filter order for the straight line cart path with moderate measurement error ($\sigma^2 = 0.1$).



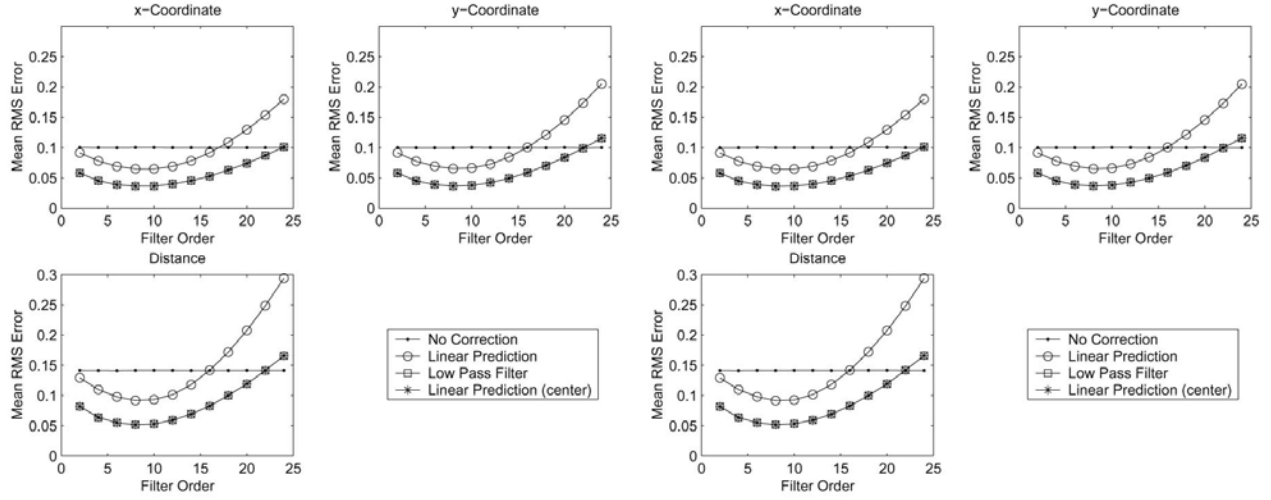
(a) Uncorrelated ($r = 0$)

(b) Moderately correlated ($r = 0.5$)



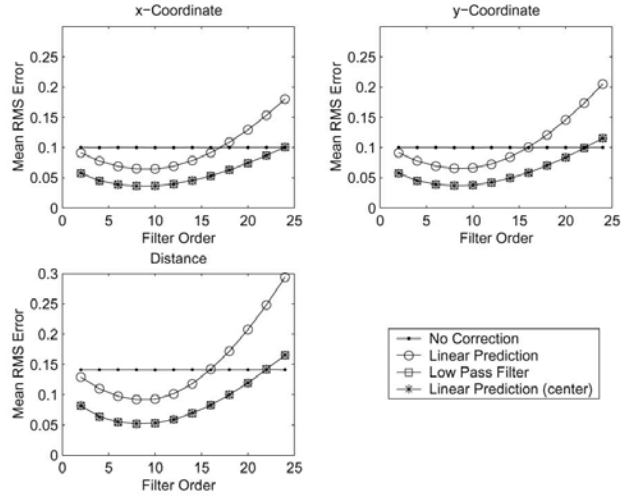
(c) Highly correlated ($r = 0.9$)

Figure 13: RMS Error as a function of filter order for the straight line cart path with high measurement error ($\sigma^2 = 1$).



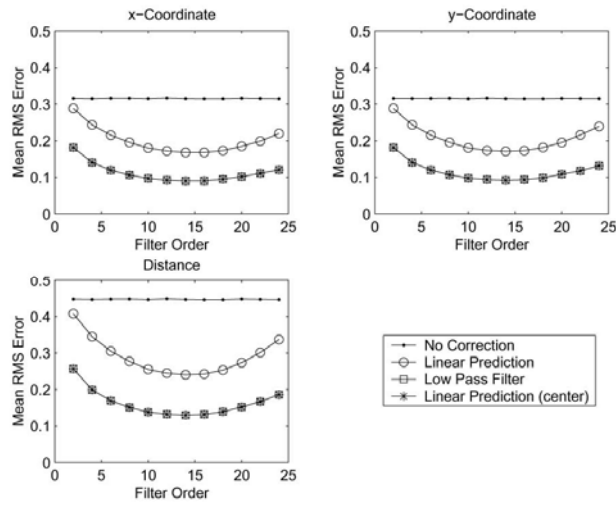
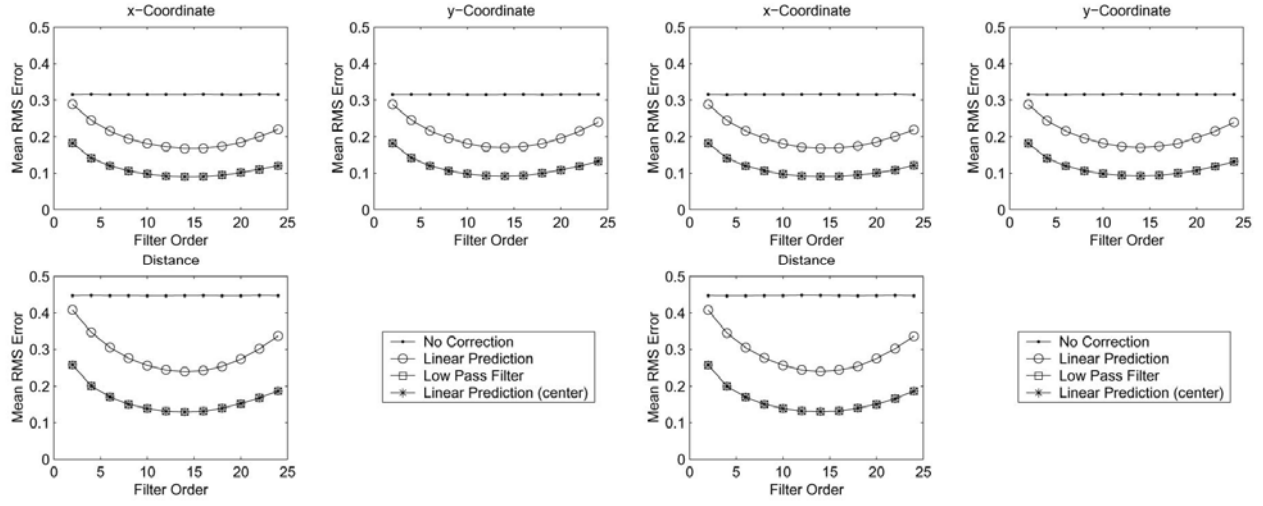
(a) Uncorrelated ($r = 0$)

(b) Moderately correlated ($r = 0.5$)



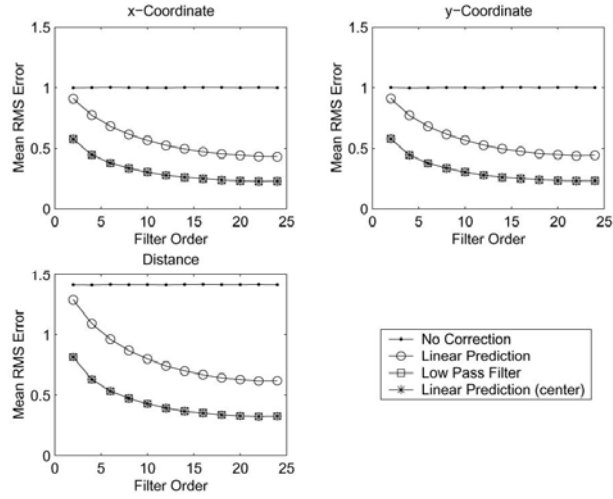
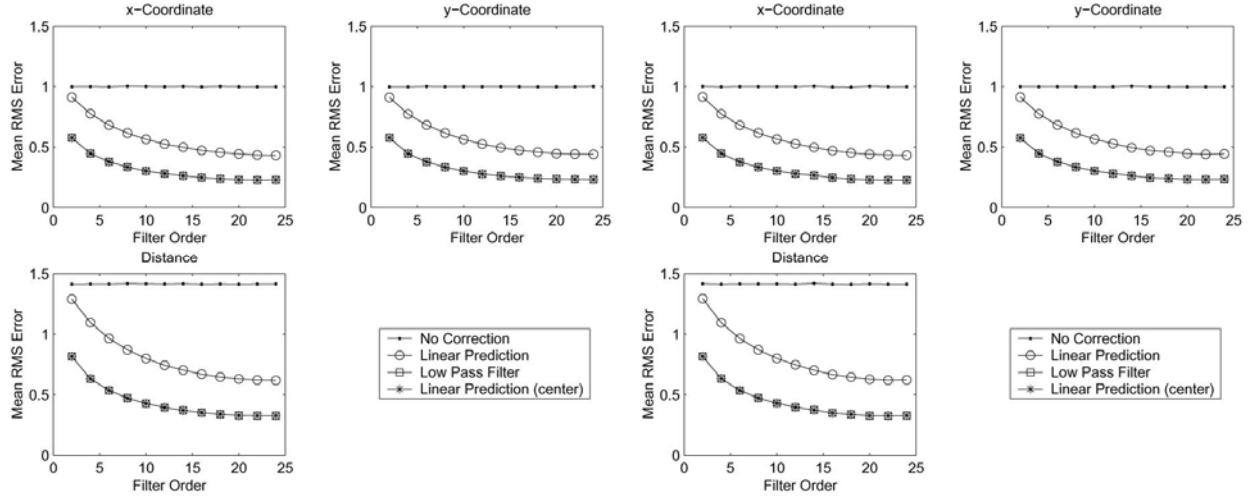
(c) Highly correlated ($r = 0.9$)

Figure 14: RMS Error as a function of filter order for the half circle cart path with low measurement error ($\sigma^2 = 0.01$).



(c) Highly correlated ($r = 0.9$)

Figure 15: RMS Error as a function of filter order for the half circle cart path with moderate measurement error ($\sigma^2 = 0.1$).



(c) Highly correlated ($r = 0.9$)

Figure 16: RMS Error as a function of filter order for the half circle cart path with high measurement error ($\sigma^2 = 1$).

4.3. Effects of Cart Path Curvature

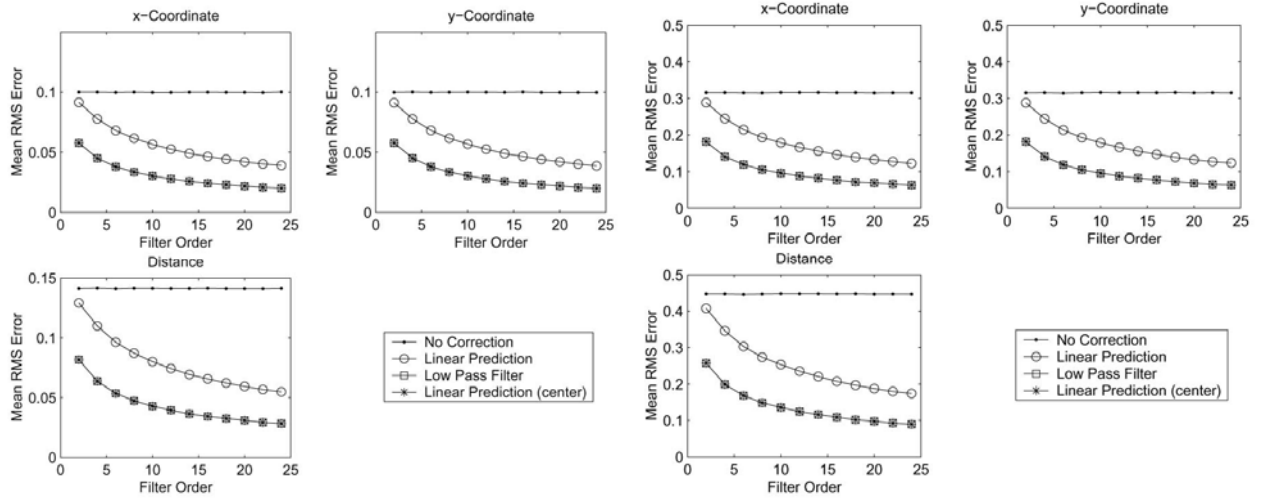
The effects of curvature in the cart path are investigated through simulations for all of the cart paths at all three error levels. Since the simulation results for the straight line and half circle cart paths showed that correlation in the measurement errors does not affect performance of the current algorithms, the simulations studying the effects of curvature in the cart path are performed only for moderately correlated errors ($r = 0.5$). The other levels of error correlation should produce the same results as those shown here.

The mean RMS errors as a function of filter order for both the x- and y-coordinates as well as overall distance are shown in Figures 17 through 27. These summary results show that the cart path curvature affects algorithm performance. As the path curvature increases (Figures 17-22), the performance degrades. This is most noticeable at the low error level ($\sigma^2 = 0.01$). In addition, it appears as though cart path curvature also affects the choice of filter order since higher filter order increases the algorithm sensitivity to curvature in the cart path.

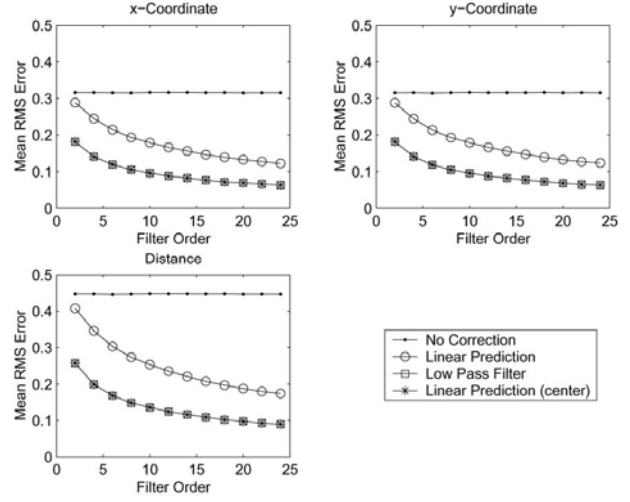
It is interesting that for the set of sinusoid paths the x- and y-coordinates often have different performance curves. This, again, is due to the curvature of the cart path. When the x- and y-coordinates are plotted versus measurement number, it can be seen that x-coordinate is more linear with measurement number than the y-coordinate. Hence, the algorithms have better performance on the x-coordinate than the y-coordinate.

To gain a better understanding of how the cart path curvature, filter order, and noise level interact, it is instructive to examine the results over the entire cart path, rather than averaging the results over the measurements. Results obtained for the 2 sinusoid cycle cart path are shown in Figures 28 through 30. These figures show the mean RMS error as a function of measurement number. The results indicate that when the noise level is low the RMS error fluctuates with the cart path curvature, so when the curvature is large, the error is large, and conversely when the curvature is small, the error is small. The larger the filter order, the more pronounced this effect. This occurs because at low noise levels, the algorithms are limited by the accuracy of the underlying model, which for these algorithms is linear. The linear assumption is least appropriate when the path curvature is large, and this produces the larger errors at those places in the path. However, at high measurement error levels, the algorithms are noise limited. When the measurement error is large, the modeling error is small in comparison. Since these algorithms either implicitly (LPF) or explicitly (linear prediction) assume a linear cart path, and they are sensitive to the accuracy of this assumption. Therefore, they are sensitive to curvature in the path, and low error level and/or large filter order increases this sensitivity.

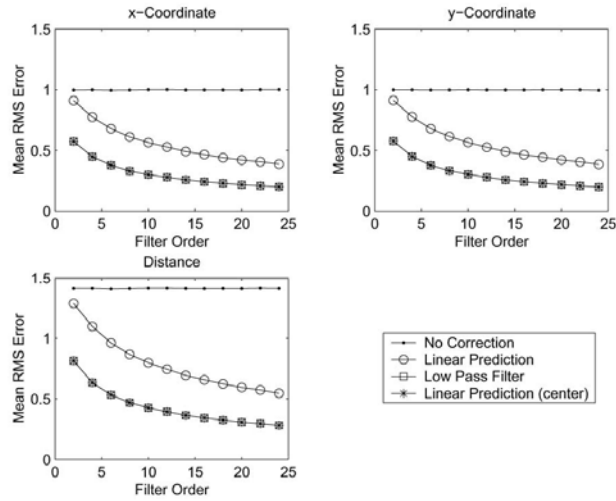
The interaction between the cart path curvature and filter order for the rectangular LPF is shown in Figure 31. These results were compiled using the straight line and circular cart paths, all of which have a constant curvature over the entire cart path. These figures clearly show that at a low noise level, where the modeling error dominates, a low filter order provides the best performance, and that at a high noise level, where the measurement error dominates, a high filter order provides the best performance. However, at a moderate noise level, where neither the modeling error nor the measurement error is dominant, the best filter order depends on the curvature of the cart path.



(a) Low noise level ($\sigma^2 = 0.01$)

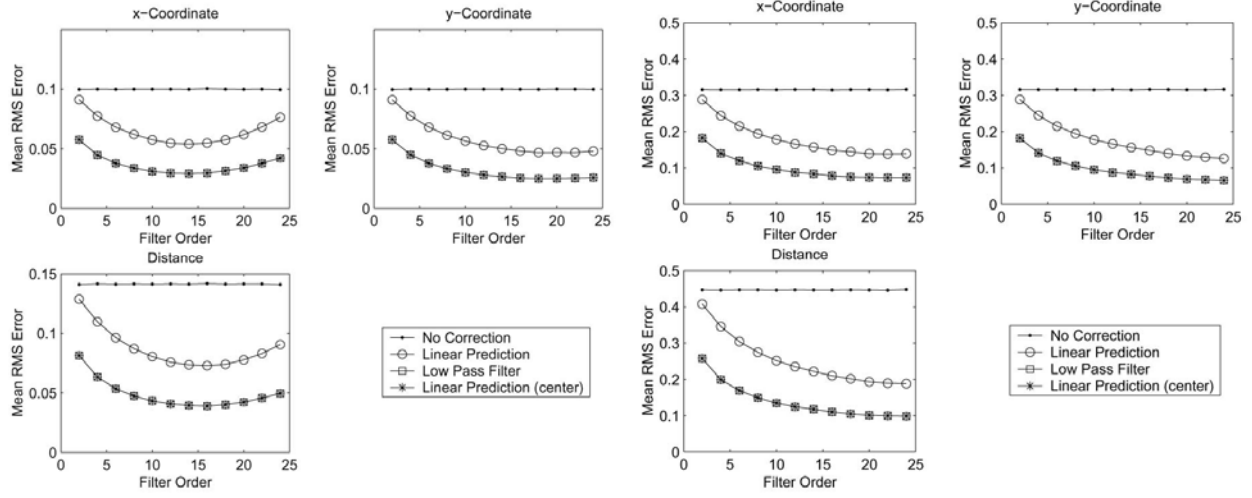


(b) Moderate noise level ($\sigma^2 = 0.1$)



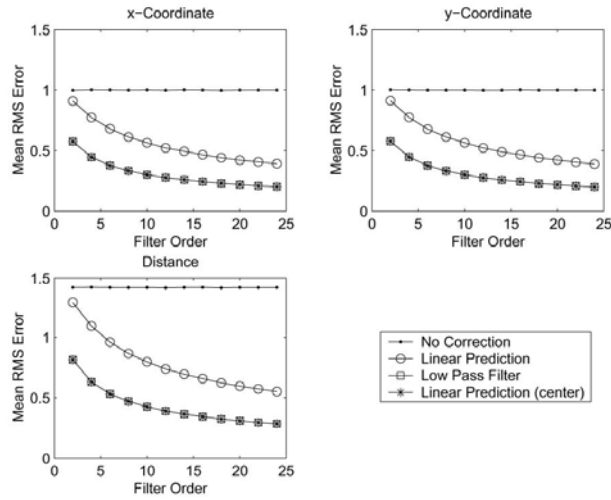
(c) High noise level ($\sigma^2 = 1$)

Figure 17: RMS Error as a function of filter order for the straight line cart path with moderate measurement error correlation ($r = 0.5$).



(a) Low noise level ($\sigma^2 = 0.01$)

(b) Moderate noise level ($\sigma^2 = 0.1$)



(c) High noise level ($\sigma^2 = 1$)

Figure 18: RMS Error as a function of filter order for the 1/8 circle cart path with moderate measurement error correlation ($r = 0.5$).

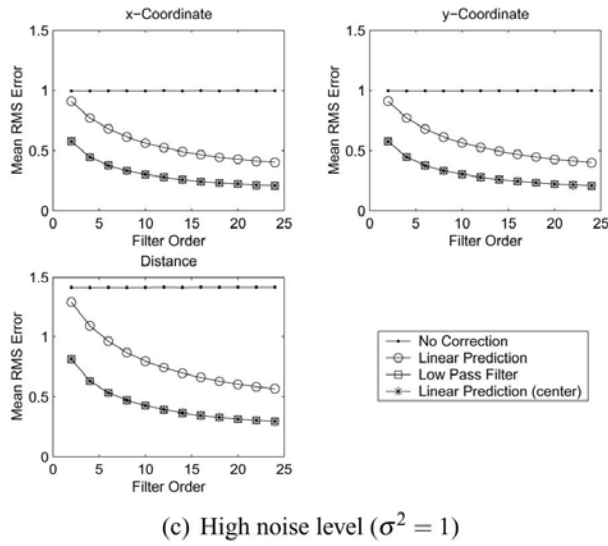
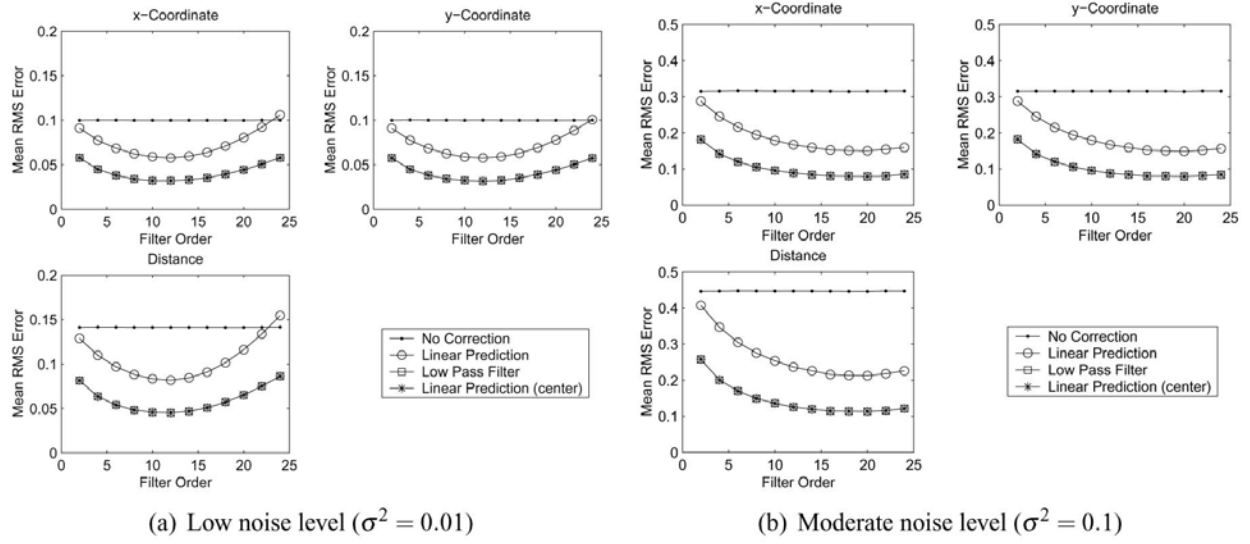


Figure 19: RMS Error as a function of filter order for the 1/4 circle cart path with moderate measurement error correlation ($r = 0.5$).

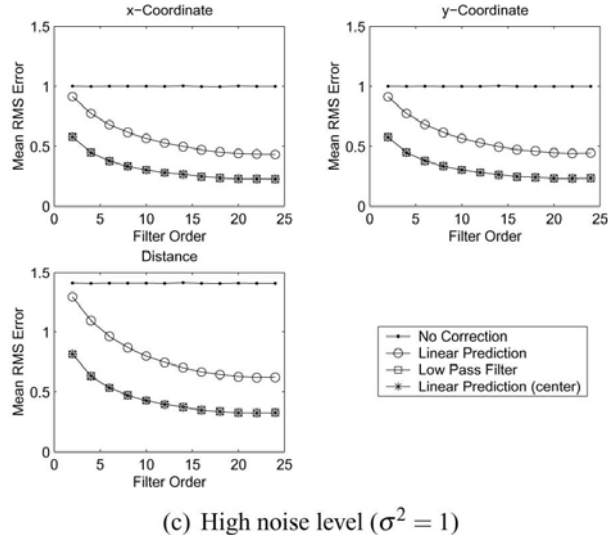
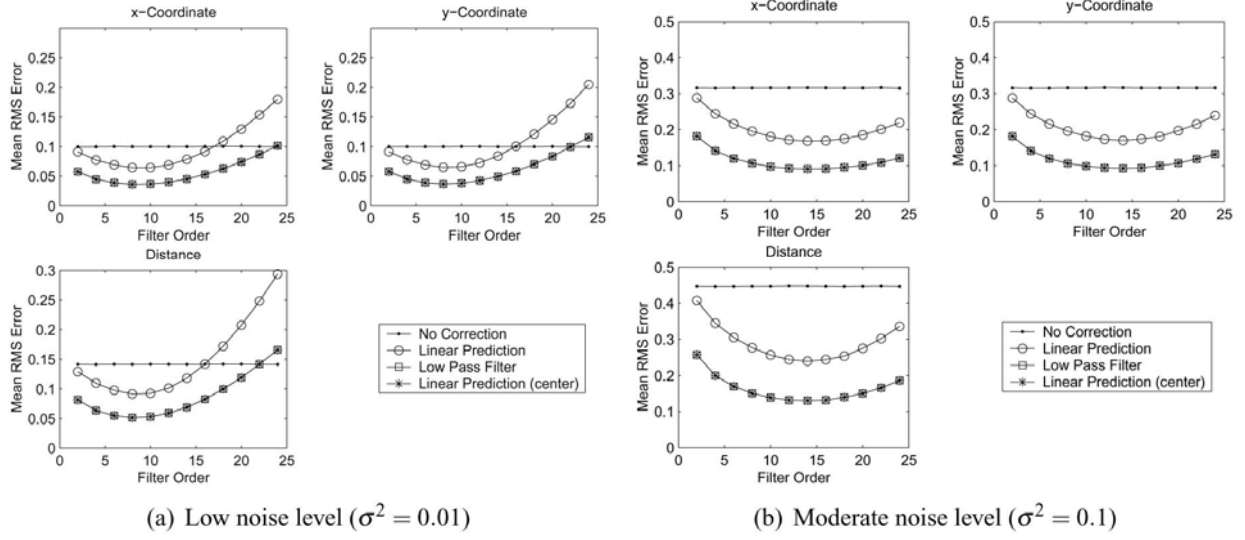
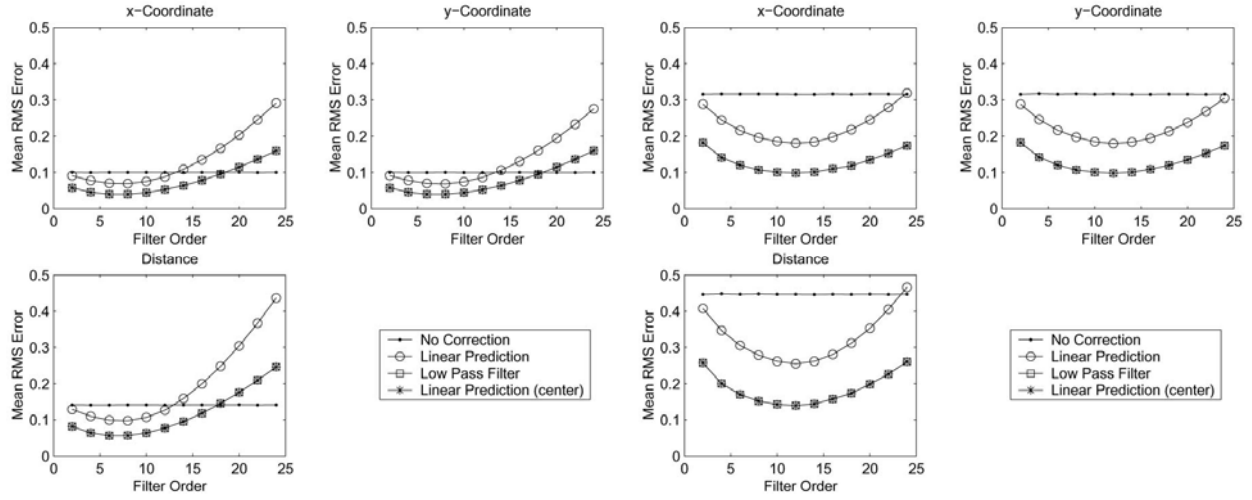
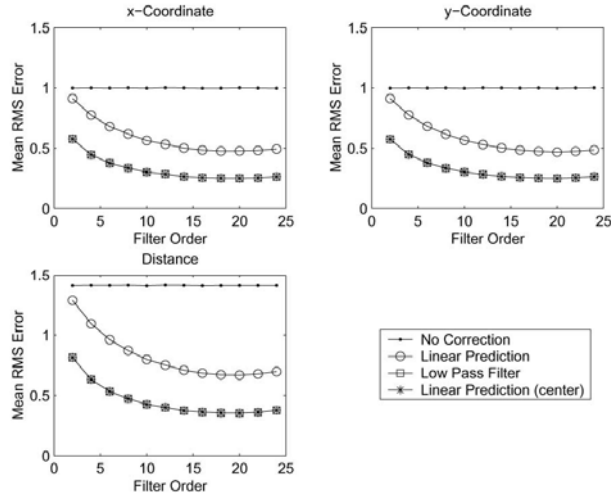


Figure 20: RMS Error as a function of filter order for the 1/2 circle cart path with moderate measurement error correlation ($r = 0.5$).



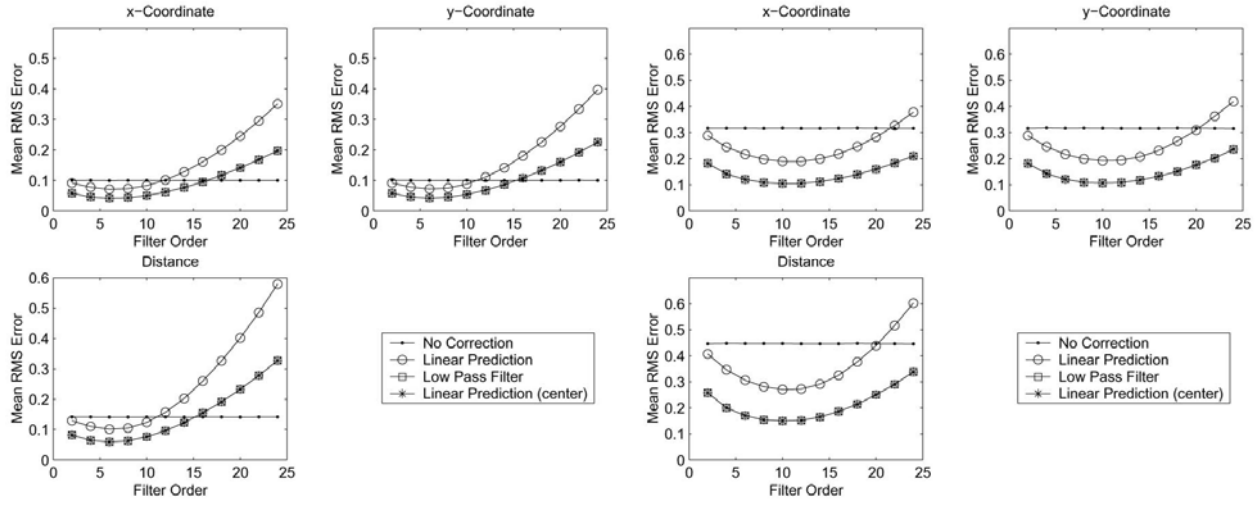
(a) Low noise level ($\sigma^2 = 0.01$)

(b) Moderate noise level ($\sigma^2 = 0.1$)

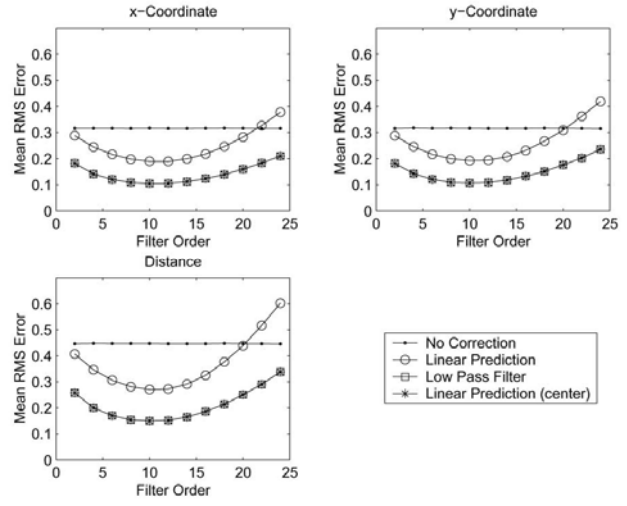


(c) High noise level ($\sigma^2 = 1$)

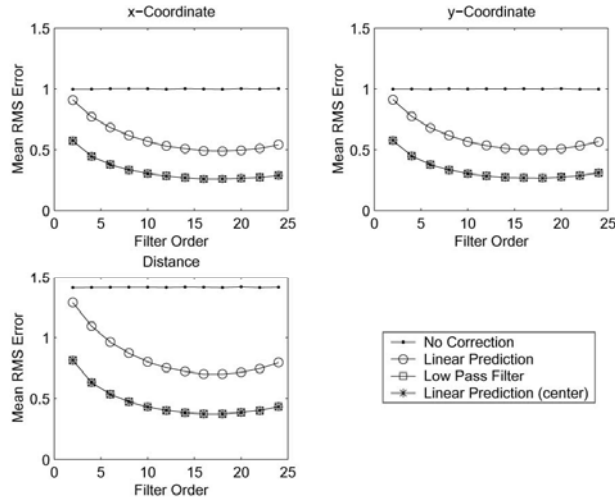
Figure 21: RMS Error as a function of filter order for the 3/4 circle cart path with moderate measurement error correlation ($r = 0.5$).



(a) Low noise level ($\sigma^2 = 0.01$)

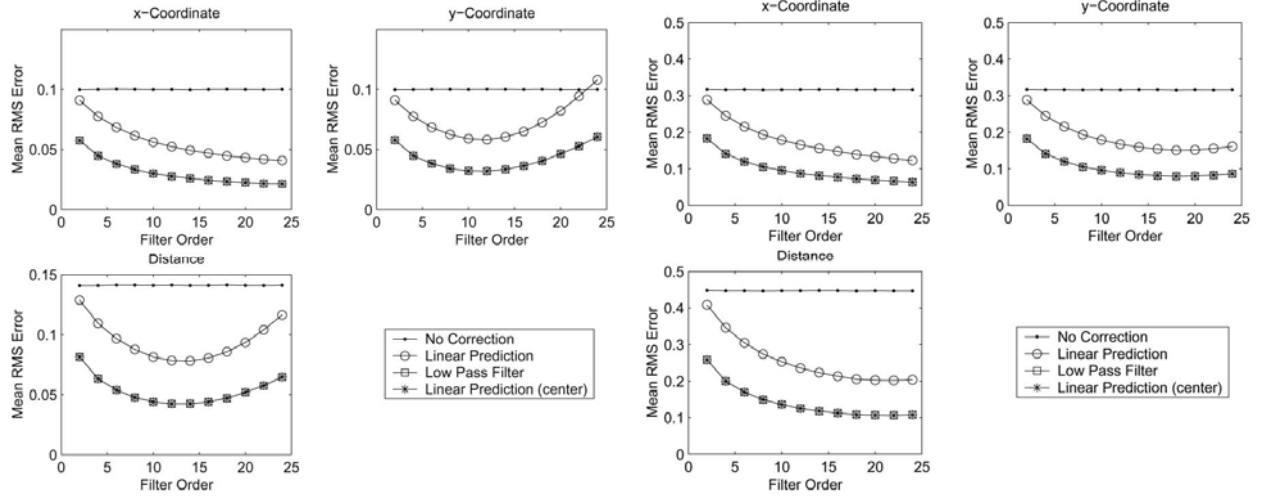


(b) Moderate noise level ($\sigma^2 = 0.1$)

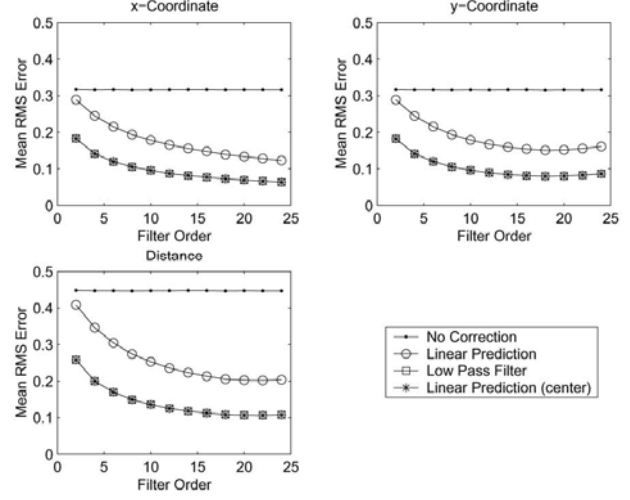


(c) High noise level ($\sigma^2 = 1$)

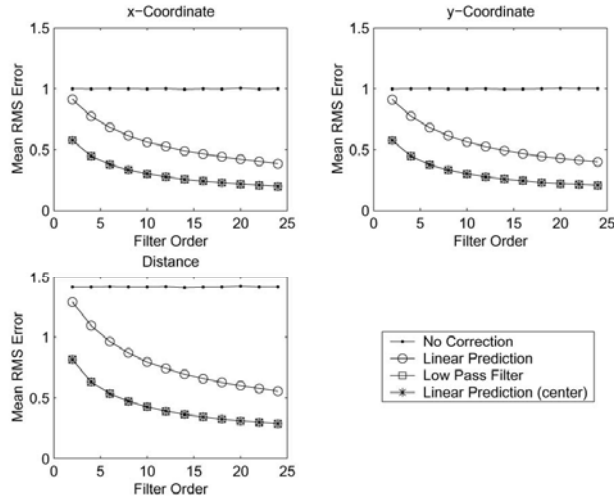
Figure 22: RMS Error as a function of filter order for the full circle cart path with moderate measurement error correlation ($r = 0.5$).



(a) Low noise level ($\sigma^2 = 0.01$)

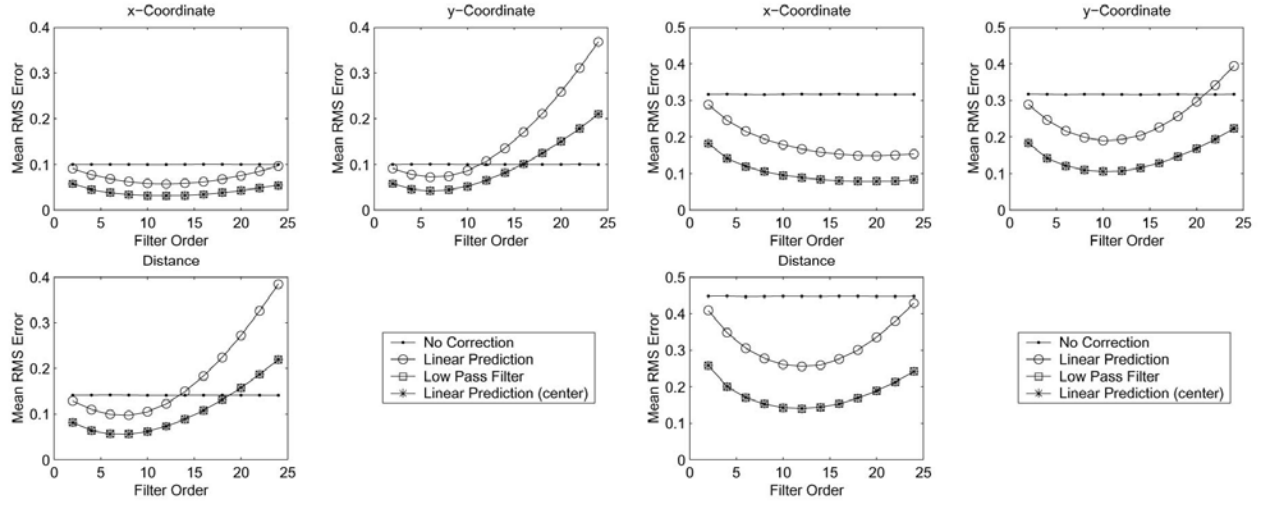


(b) Moderate noise level ($\sigma^2 = 0.1$)



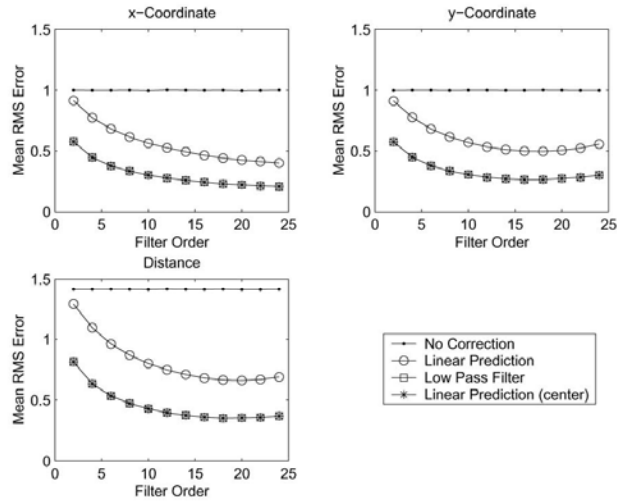
(c) High noise level ($\sigma^2 = 1$)

Figure 23: RMS Error as a function of filter order for the 1 sinusoid cycle cart path with moderate measurement error correlation ($r = 0.5$).



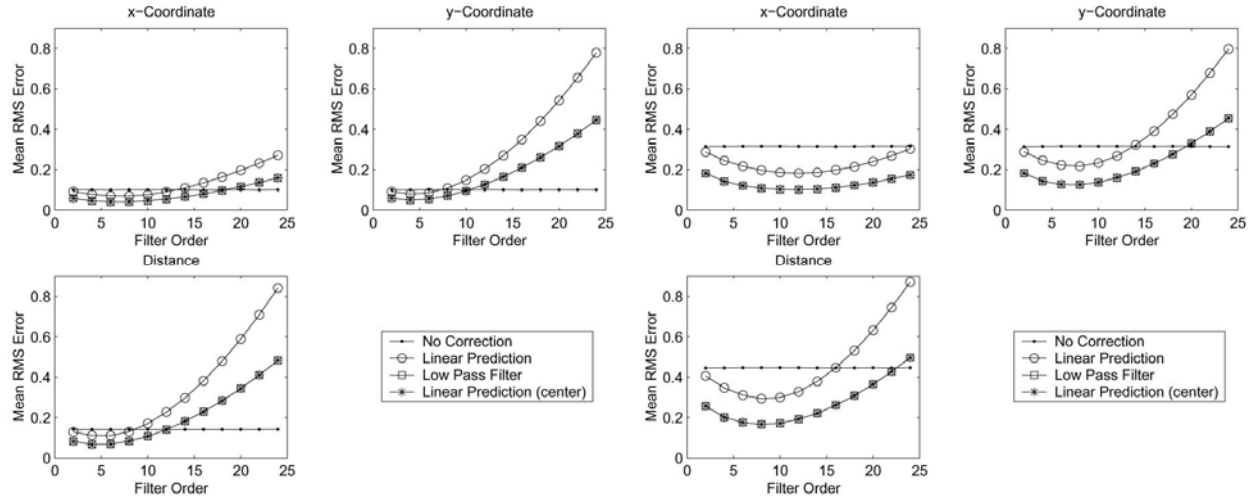
(a) Low noise level ($\sigma^2 = 0.01$)

(b) Moderate noise level ($\sigma^2 = 0.1$)



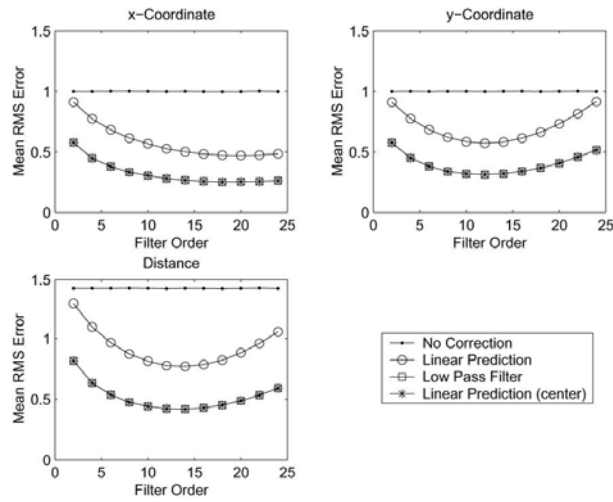
(c) High noise level ($\sigma^2 = 1$)

Figure 24: RMS Error as a function of filter order for the 2 sinusoid cycle cart path with moderate measurement error correlation ($r = 0.5$).



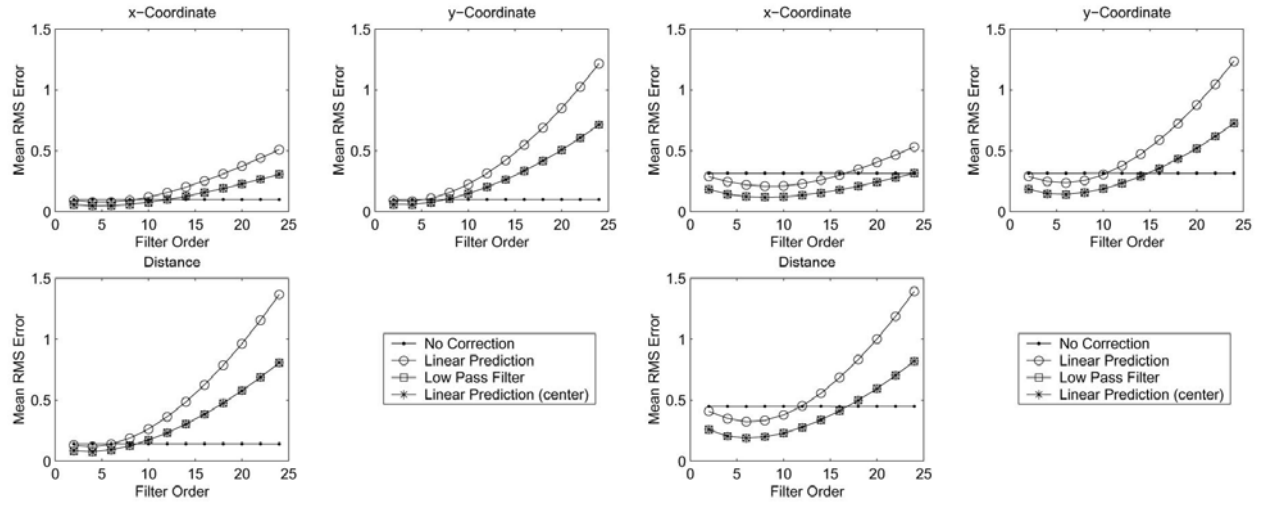
(a) Low noise level ($\sigma^2 = 0.01$)

(b) Moderate noise level ($\sigma^2 = 0.1$)



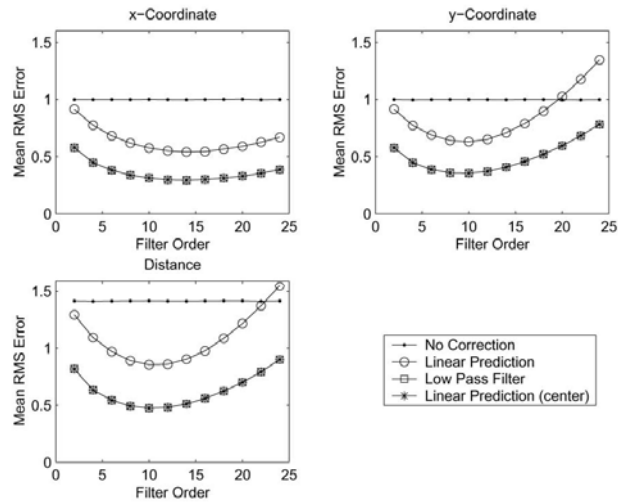
(c) High noise level ($\sigma^2 = 1$)

Figure 25: RMS Error as a function of filter order for the 3 sinusoid cycle cart path with moderate measurement error correlation ($r = 0.5$).



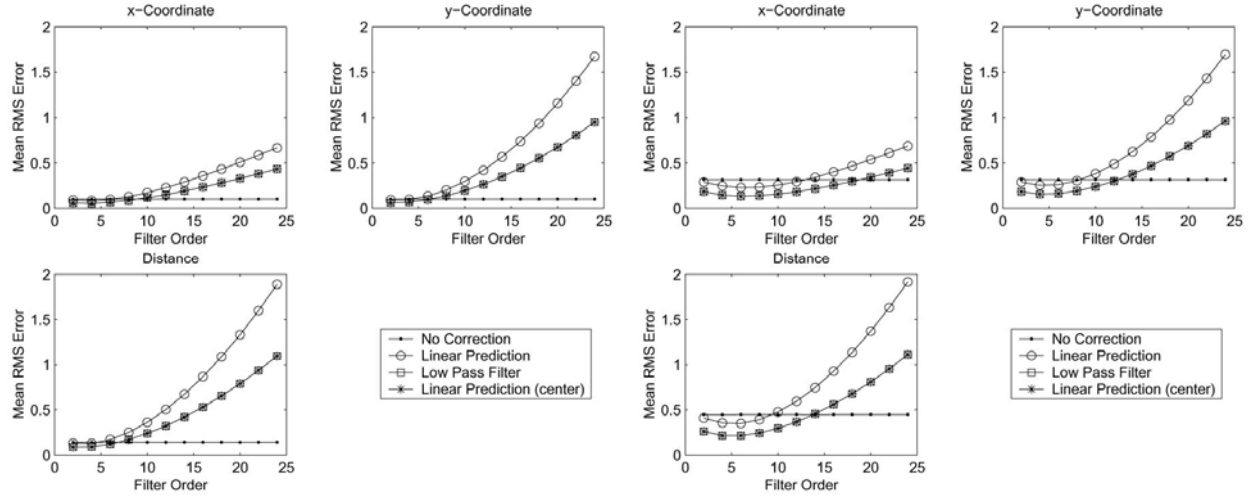
(a) Low noise level ($\sigma^2 = 0.01$)

(b) Moderate noise level ($\sigma^2 = 0.1$)



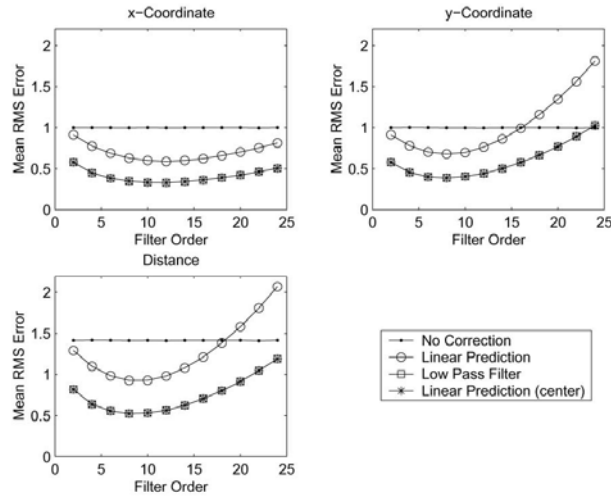
(c) High noise level ($\sigma^2 = 1$)

Figure 26: RMS Error as a function of filter order for the 4 sinusoid cycle cart path with moderate measurement error correlation ($r = 0.5$).



(a) Low noise level ($\sigma^2 = 0.01$)

(b) Moderate noise level ($\sigma^2 = 0.1$)



(c) High noise level ($\sigma^2 = 1$)

Figure 27: RMS Error as a function of filter order for the 5 sinusoid cycle cart path with moderate measurement error correlation ($r = 0.5$).

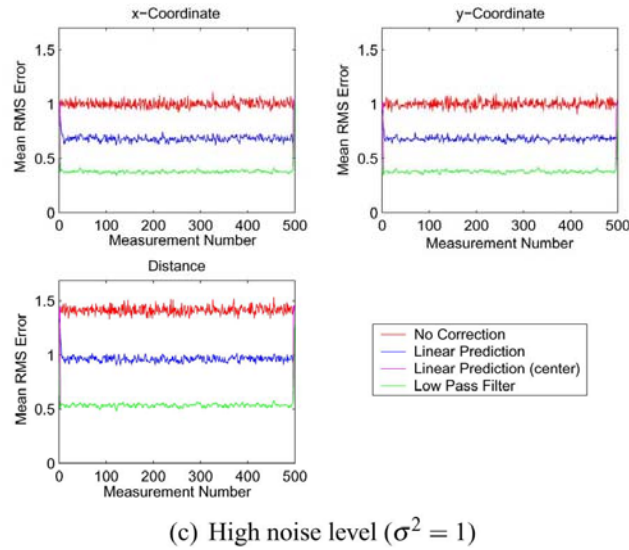
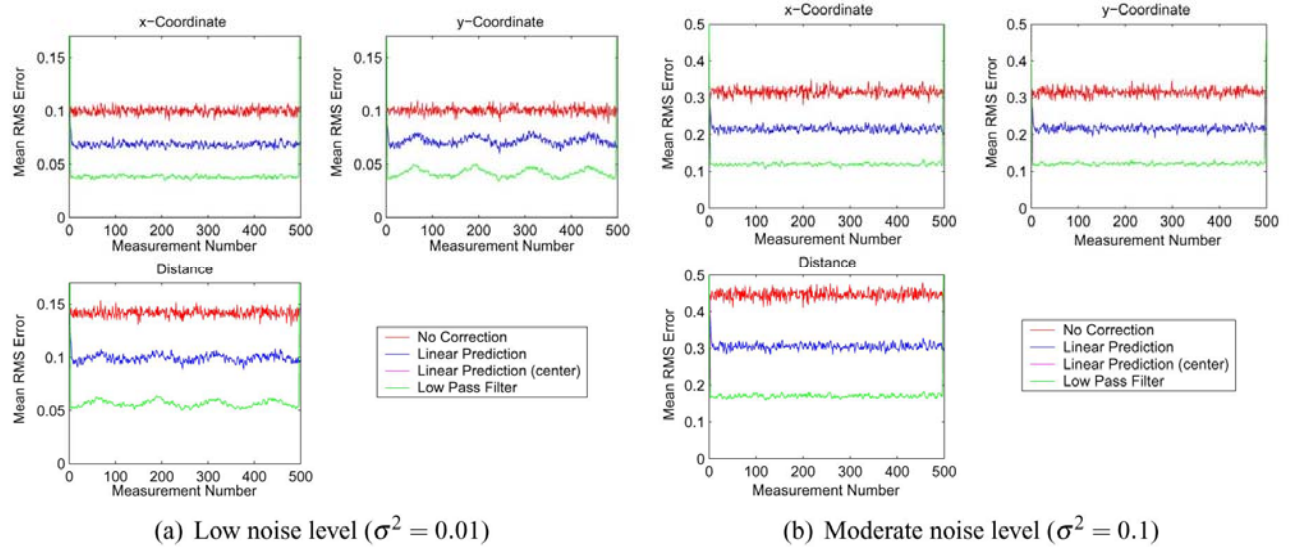


Figure 28: RMS Error as a function of measurement number with moderate measurement error correlation ($r = 0.5$) for the 2 sinusoid cycle cart path and filter order of 6.

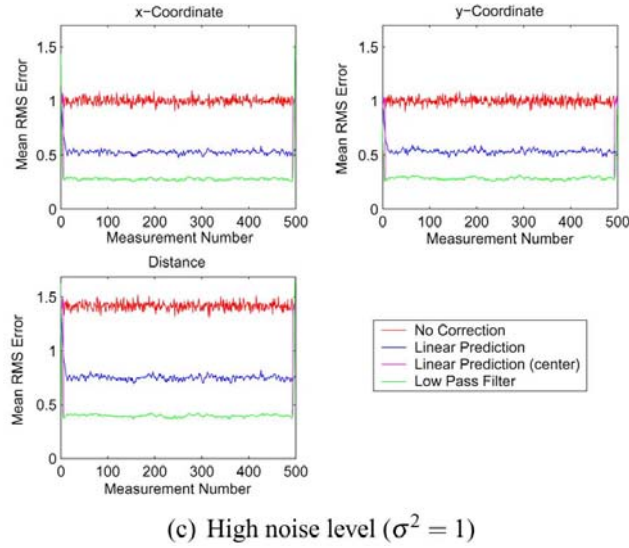
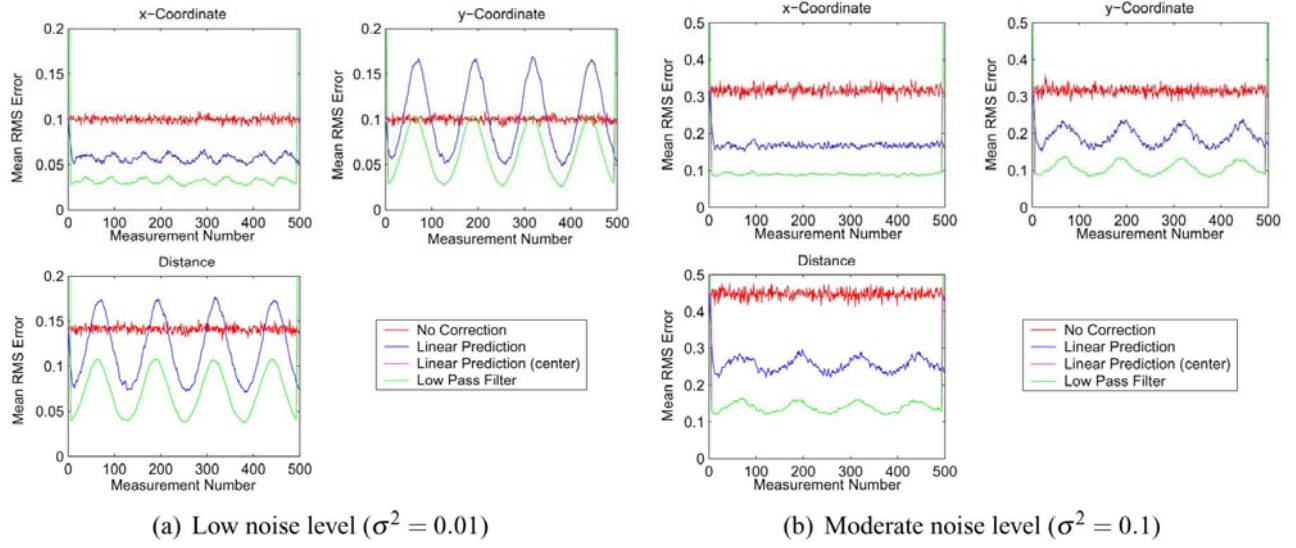


Figure 29: RMS Error as a function of measurement number with moderate measurement error correlation ($r = 0.5$) for the 2 sinusoid cycle cart path and filter order of 12.

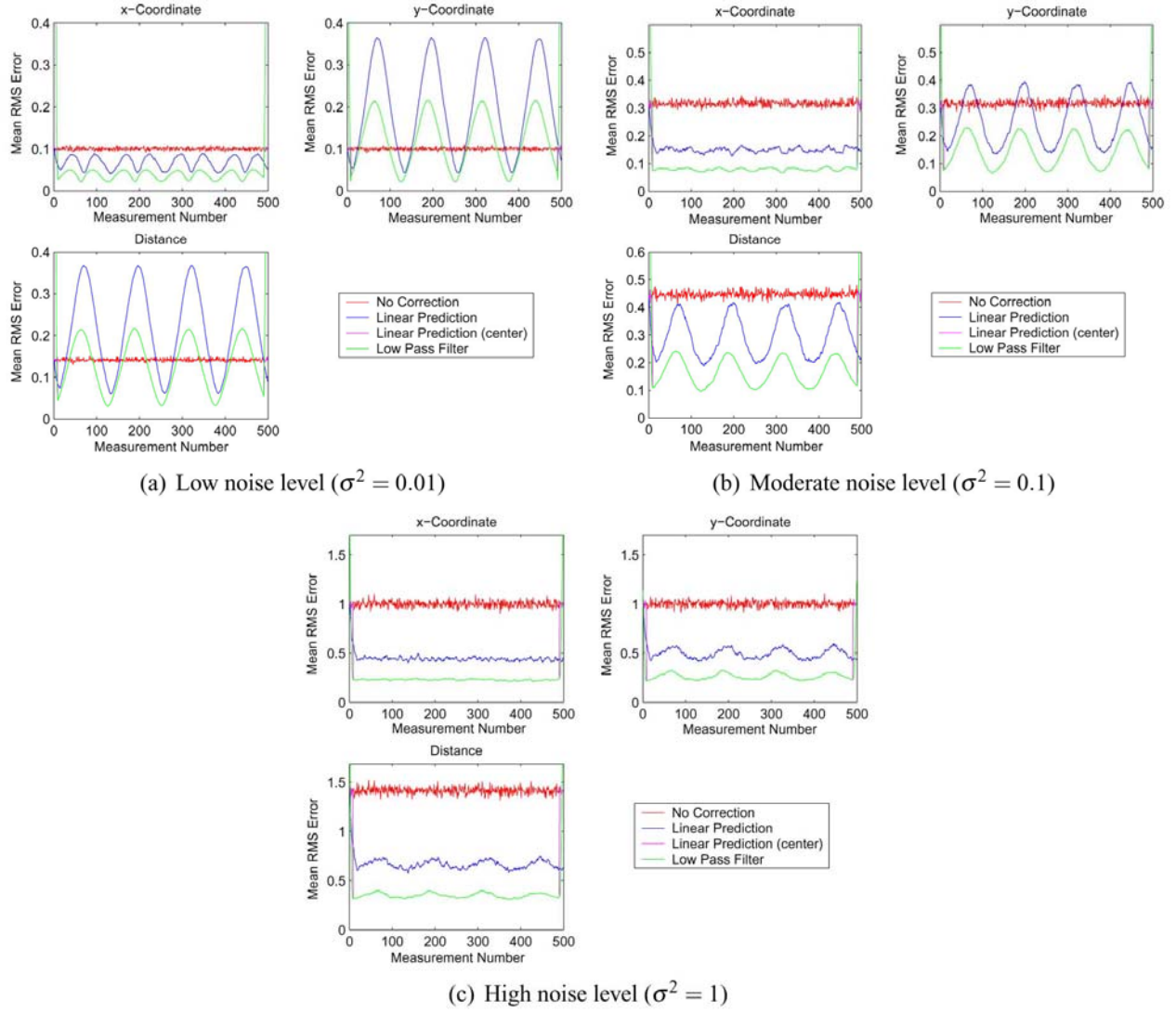
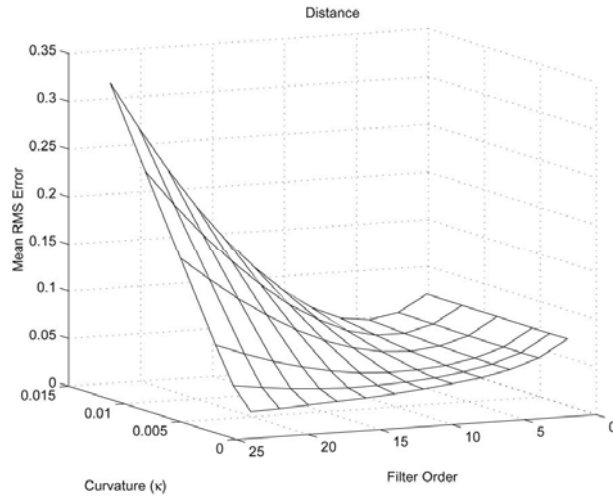
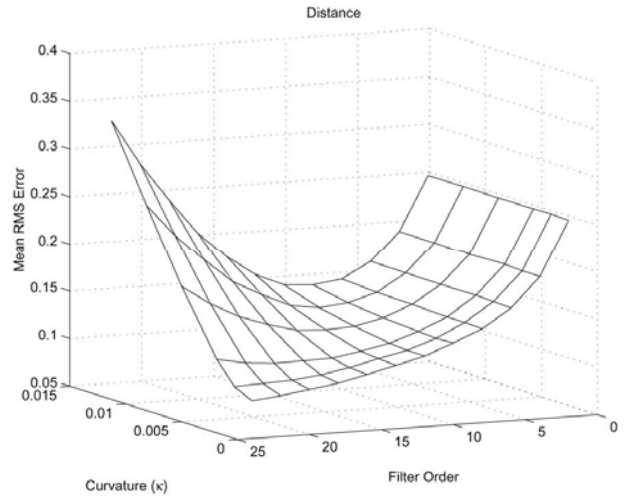


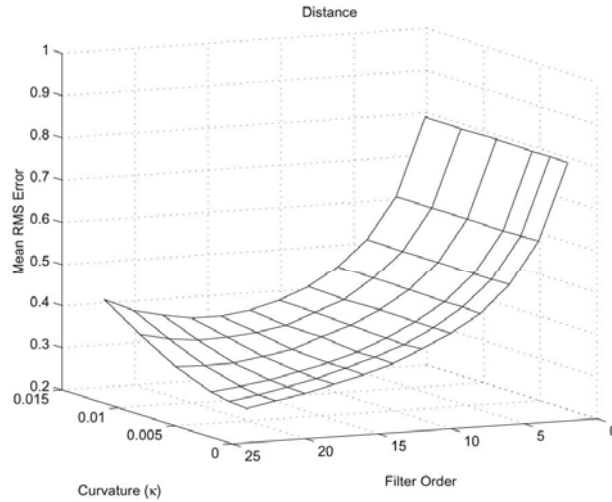
Figure 30: RMS Error as a function of measurement number with moderate measurement error correlation ($r = 0.5$) for the 2 sinusoid cycle cart path and filter order of 18.



(a) Low noise level ($\sigma^2 = 0.01$)



(b) Moderate noise level ($\sigma^2 = 0.1$)



(c) High noise level ($\sigma^2 = 1$)

Figure 31: RMS Error produced by the rectangular low-pass filter as a function of path curvature and filter order for the straight line and circular cart paths with moderate measurement error correlation ($r = 0.5$).

For cart paths which do not have constant curvature, such as the sinusoidal paths considered in these simulations, the choice of filter order is more difficult since low filter order is appropriate for some segments while high filter order is appropriate for other segments. It is anticipated that future (adaptive) algorithms will provide better performance not only for paths with some constant curvature, but also for paths with varying curvature.

4.4. Impact of Cart Motion Characterization

The impact of characterizing the cart path prior to applying error-correction algorithms to the GPS measurements is evaluated through simulations. For comparison, an LPF of order 6 is also evaluated in these simulations. The cart path utilized in the simulations is the simulated path shown in Figure 3. In these simulations, the error variances in the x- and y-directions range from $\sigma^2 = 1 \times 10^{-6}$ to $\sigma^2 = 1 \times 10^{-3}$. These error levels are smaller than those used previously because the distance between successive samples is now .05m, rather than 1m.

First, the HMM is applied to the first difference in the GPS measurements to estimate the state sequence. The most likely state sequence is determined using the Viterbi algorithm, and that state sequence is then used to guide the error correction. If the estimated state is one of the forward motion states, an LPF of order 6 is applied to reduce the GPS measurement errors. The filter order is reduced at the boundaries of the cart path segment so that measurements associated with a different type of motion do not impact the error correction of the current segment. The estimated state sequence is used to define the boundaries of the different segments in the cart path. Thus, the HMM not only allows us to apply an appropriate filter to the different segments of the cart path, but it also allows us to transition between the segments in an appropriate way. If the estimated state is one of the detour or turn around states, an LPF of order 2 is applied to reduce the GPS measurement errors. The lower filter order removes the major perturbations in the GPS measurements, while not imposing a linear model over a long series of measurements. This filter order is chosen for the detours because it is anticipated that the detours seen in real data will be more gently curved, and not the idealized straight line segments utilized in these simulations.

Single realization simulation results are shown for a range of error variances in Figures 32 through 38 (low variance to high variance). The top panel in each of these figures shows the noisy measurements (green dots), the corrected measurements using the HMM (red circles), and the corrected measurements using the LPF (cyan squares) for the entire cart path. The bottom panels each show sections of the cart path in more detail. The left bottom panel shows a turn around and perturbations induced by cart tilt, and the right bottom panel shows detours as well as a straight line segment.

The bottom panels illustrate the differences between the using the HMM and only the LPF on the GPS error correction at the boundaries between the straight line motion and the nonlinear motion (detour or turn around). At low and moderate noise variances, where the modeling errors resulting from assuming strictly linear motion dominate the LPF results, the HMM outperforms the LPF. At high noise variances, where the noise dominates the LPF results, the LPF outperforms the HMM. The exception to these observations is where cart tilt introduces perturbations in the cart path. At these locations, the LPF outperforms the HMM for all error levels because the HMM is incorrectly characterizing these segments as small detours. This

illustrates the sensitivity of the HMM approach to the accuracy of the model. If the detour model forced the detours to be at least farther away from the forward motion segment than the perturbation induced by the cart tilt, it is likely those segments would be correctly characterized as forward motion. This hypothesis will be evaluated in future simulations.

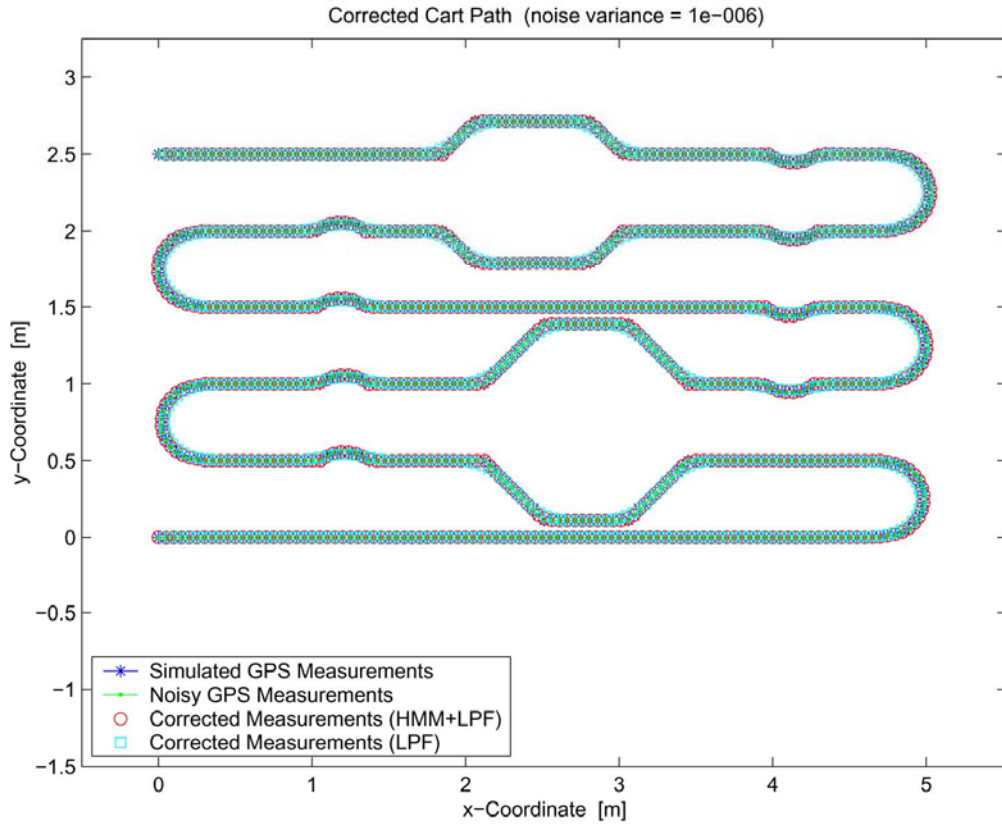
The above observations are quantified in Figure 39. The figure summarizes the results obtained for 100 independent realizations of noisy GPS measurements. It shows the mean RMS error across all measurements as a function of the GPS measurement error variance. The mean RMS errors increase as the measurement error variance increases, as expected. It is interesting to note that the HMM has lower mean RMS error than the LPF for low measurement error variance; however, the LPF has lower mean RMS error than the HMM for high measurement error variance. These are consistent with the observations made about the corrected cart paths for the single realization results.

5. Real Data Processing: ATD/JPG

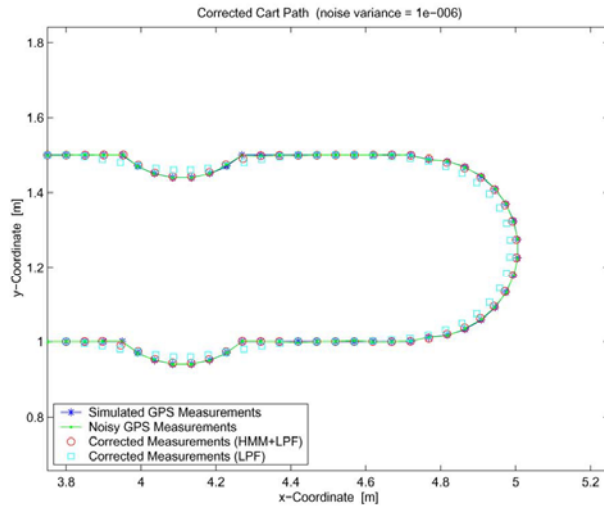
The GPS error correction algorithm is validated using data collected at the ATD/JPG, and the results are shown in Figure 40. Some of the algorithm parameters were adjusted to better match the measurement conditions in this data collection. For instance, the distance between successive measurements was increased from 0.05m to 0.125m. In addition, the cart motion model was modified to force the detours to be further away from the straight line path by adding more states to the movement away from and back toward the forward motion state.

While there were volumes of data collected, and processed, only a representative subset is shown in Figure 40. This section of the cart path was chosen because it illustrates some interesting features. Since ground truth is not available for this data set, the performance evaluation is more qualitative than quantitative. In the section at approximately $(x,y) = (-0.75, 20.75)$, both the LPF and the HMM followed by filtering remove the bump seen in the measured data. This is a section where the HMM characterized the cart motion as linear, and attributes the deviation in the GPS measurements to the cart tilting. However, in the section at approximately $(x,y) = (-2.75, 20.75)$, the HMM follows the measured data, while the LPF alone deviates significantly from it. In this section, the HMM characterized the cart motion as the beginning of the turn around. Finally, the turn around section shows that the LPF alone introduces a systematic error, while the HMM continues to follow the measured data.

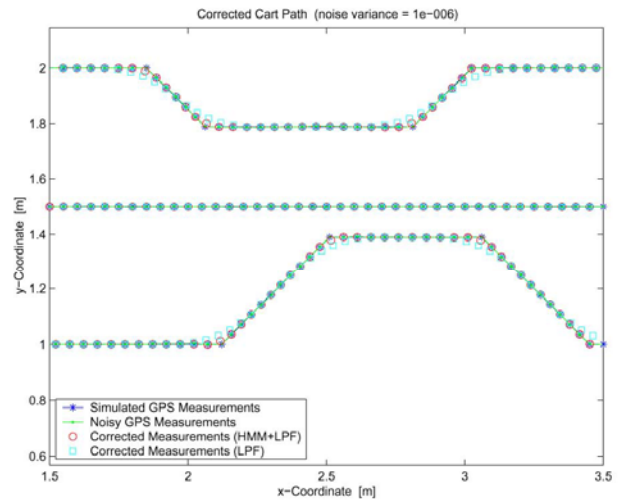
Although the HMM approach, in this case, appears qualitatively to have done a better job at error correcting than the LPF alone, the approach is far from robust in its current configuration. The major source of contention is usually the incorrect characterization of perturbations in the cart path (due to tilting) as small detours in the cart path. A logical way to resolve this ambiguity is to track the orientation of the cart as it moves over the uneven terrain.



(a) Corrected cart path.

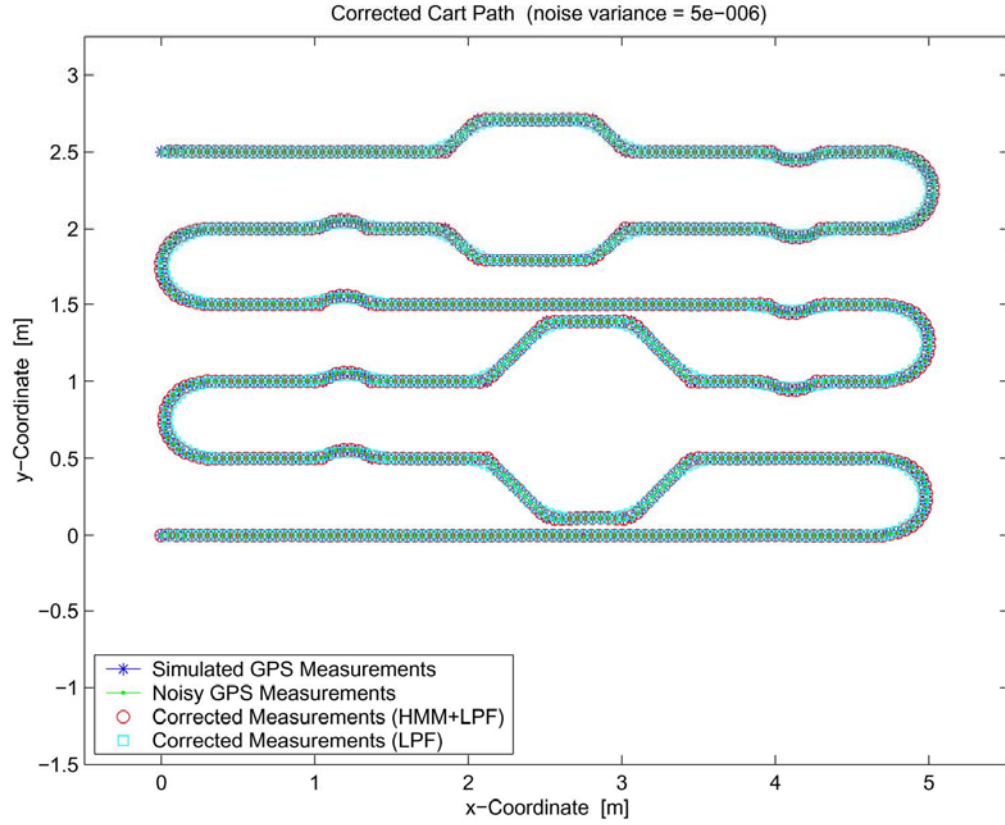


(b) Detail of turn around and cart tilt.

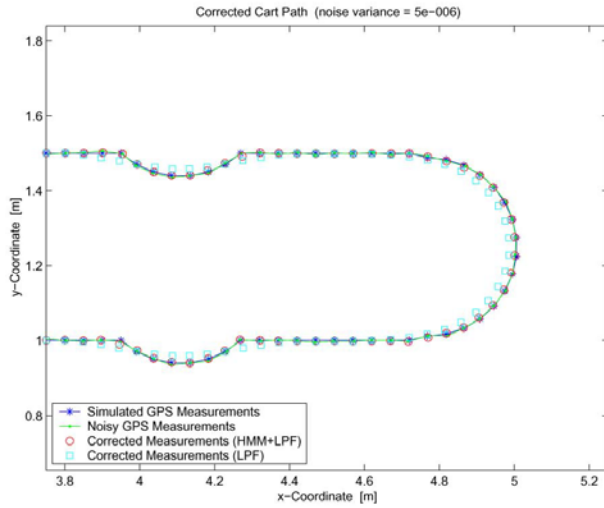


(c) Detail of obstacle avoidance and straight line.

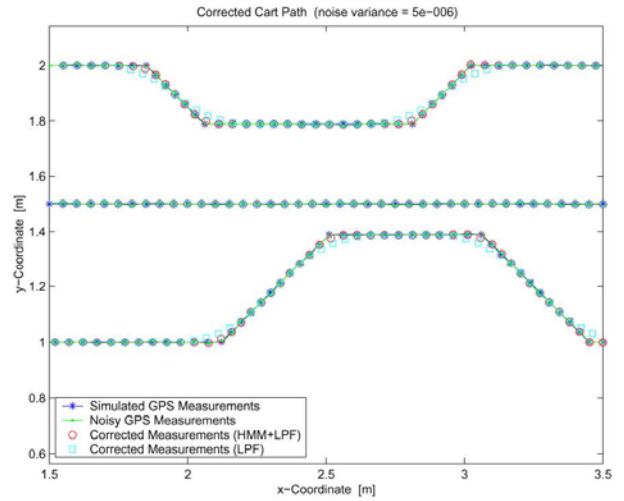
Figure 32: Simulated cart path with noisy GPS measurements and error-corrected GPS measurements for measurement error variance $\sigma^2 = 1 \times 10^{-6}$.



(a) Corrected cart path.

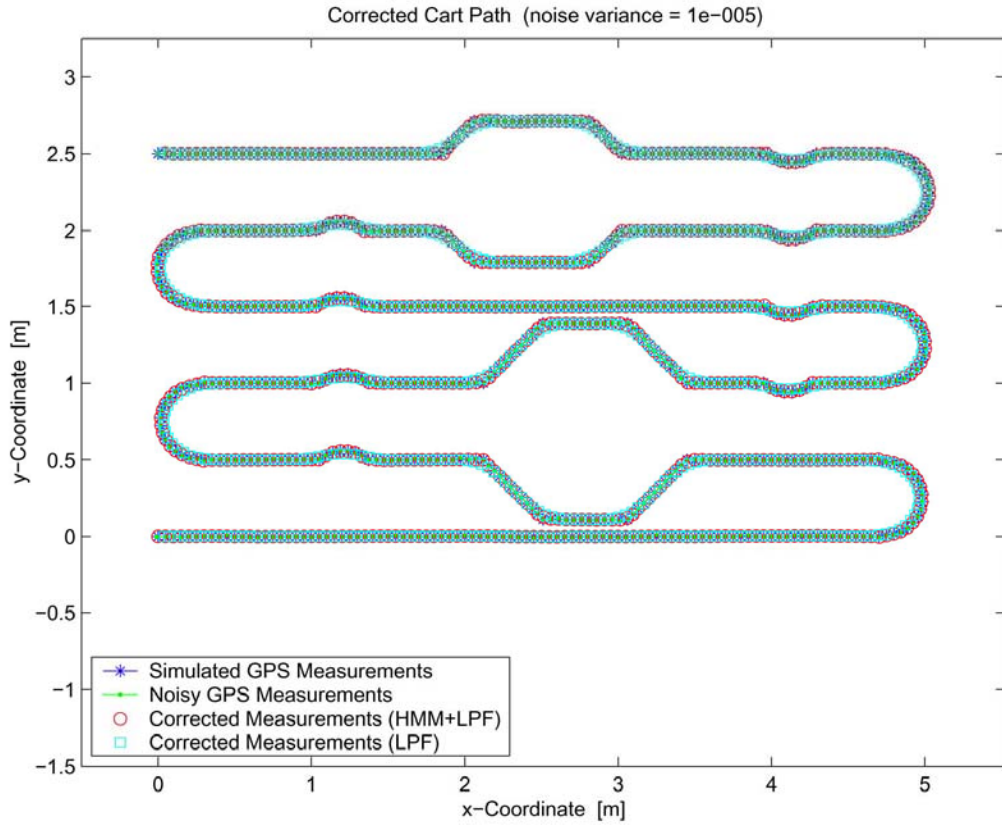


(b) Detail of turn around and cart tilt.

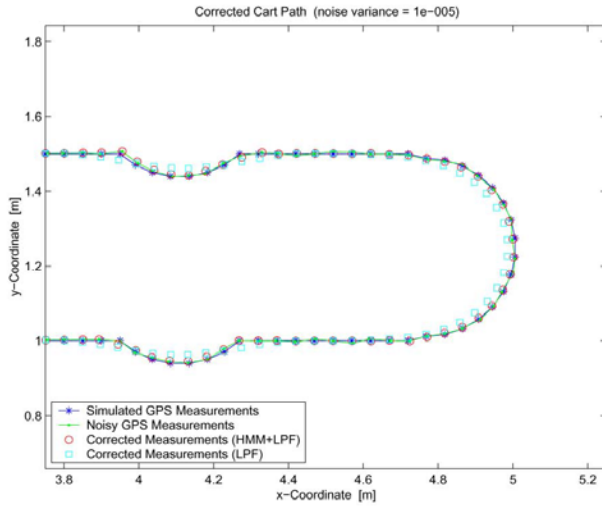


(c) Detail of obstacle avoidance and straight line.

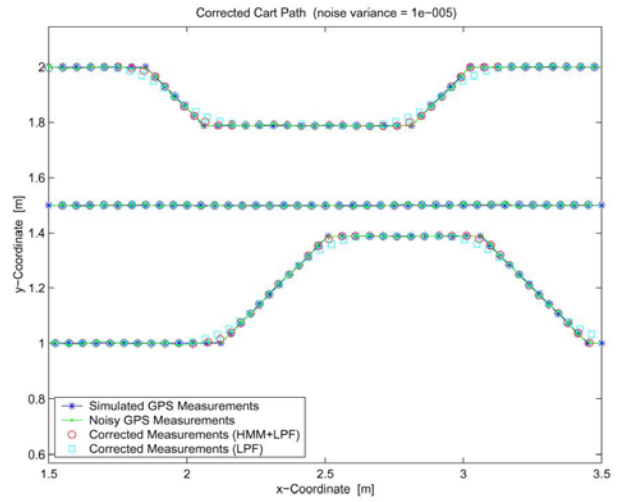
Figure 33: Simulated cart path with noisy GPS measurements and error-corrected GPS measurements for measurement error variance $\sigma^2 = 5 \times 10^{-5}$.



(a) Corrected cart path.

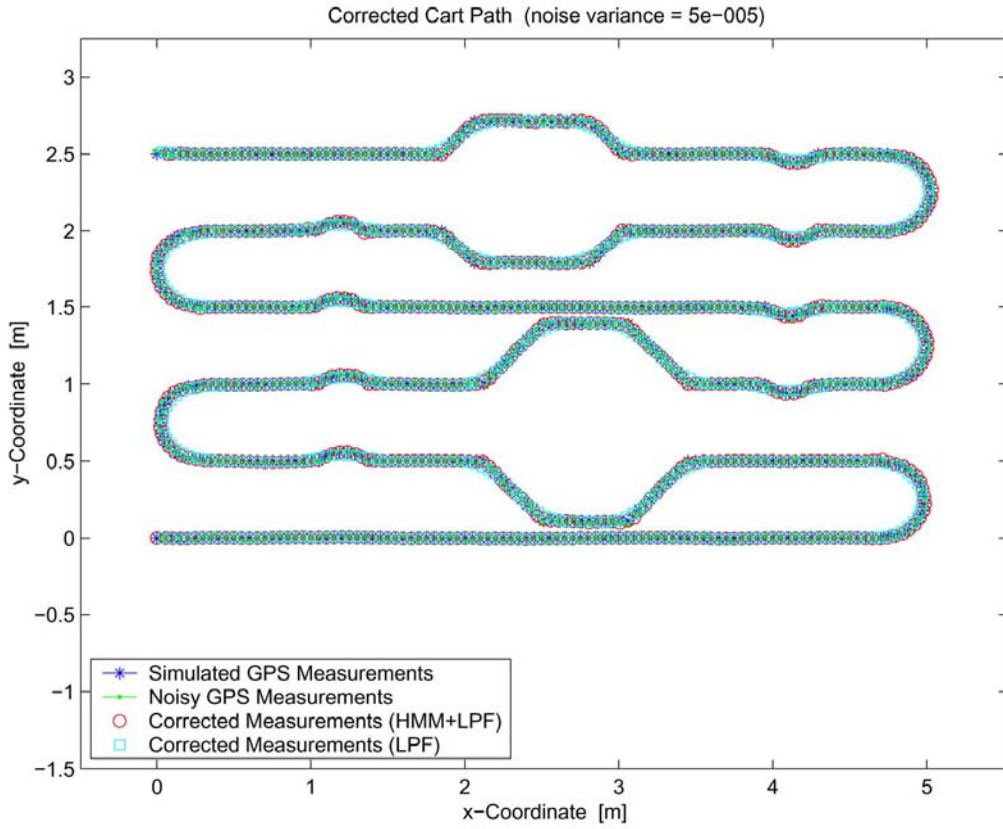


(b) Detail of turn around and cart tilt.

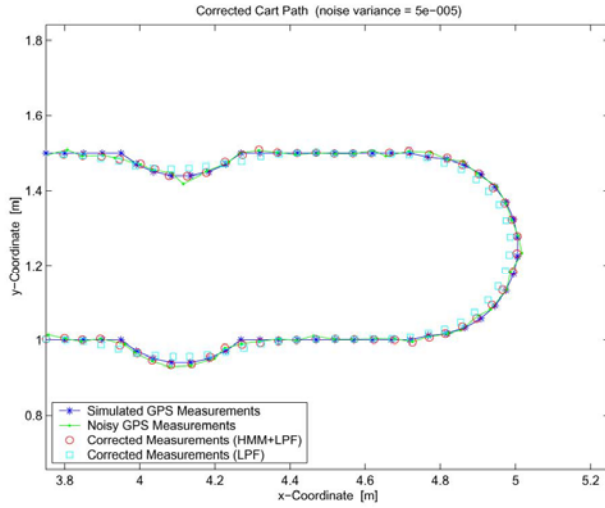


(c) Detail of obstacle avoidance and straight line.

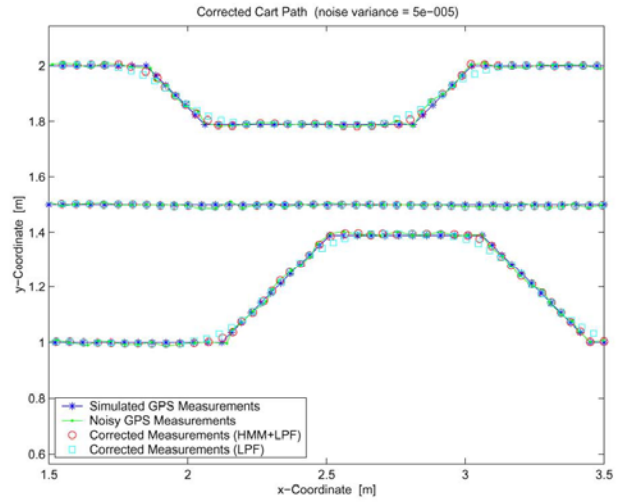
Figure 34: Simulated cart path with noisy GPS measurements and error-corrected GPS measurements for measurement error variance $\sigma^2 = 1 \times 10^{-5}$.



(a) Corrected cart path.

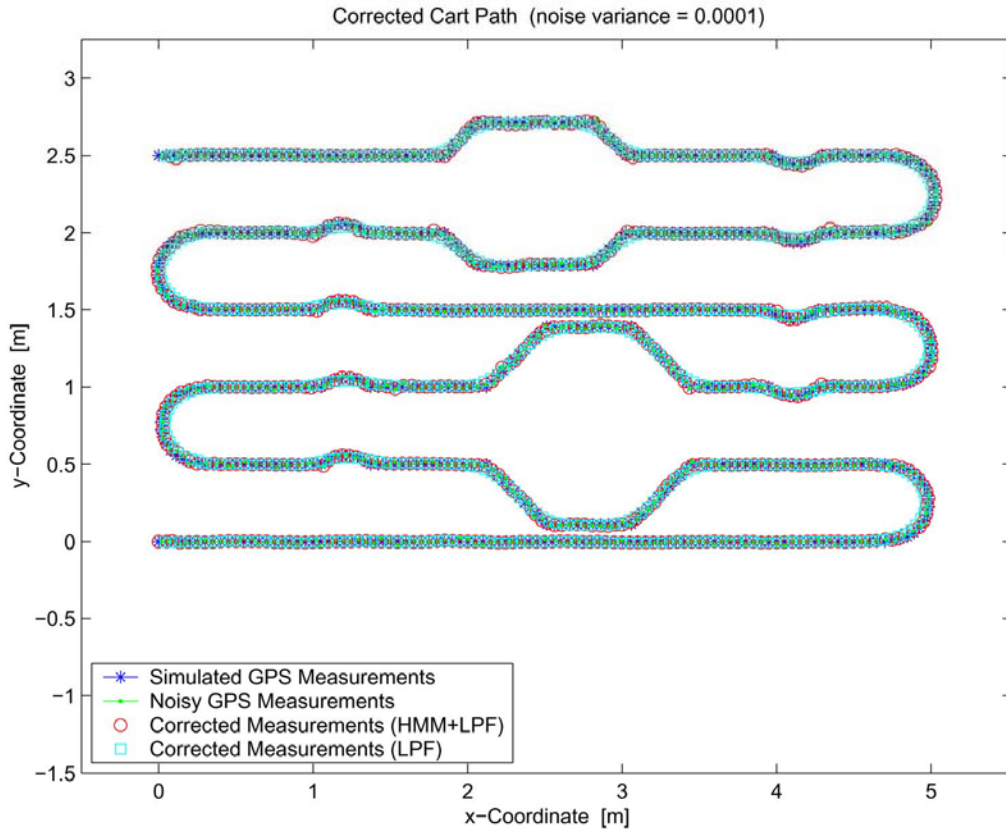


(b) Detail of turn around and cart tilt.

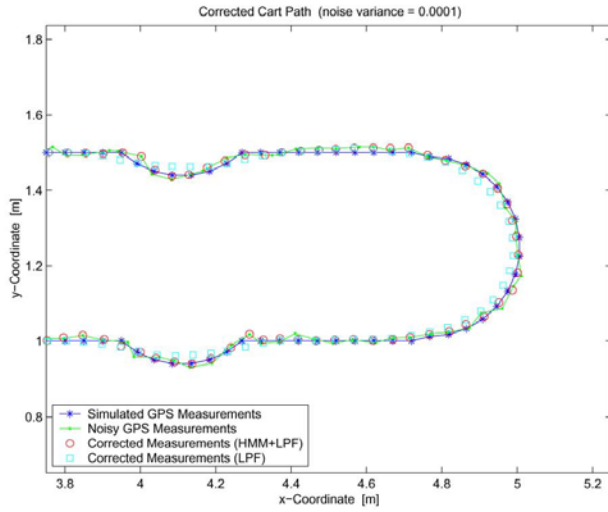


(c) Detail of obstacle avoidance and straight line.

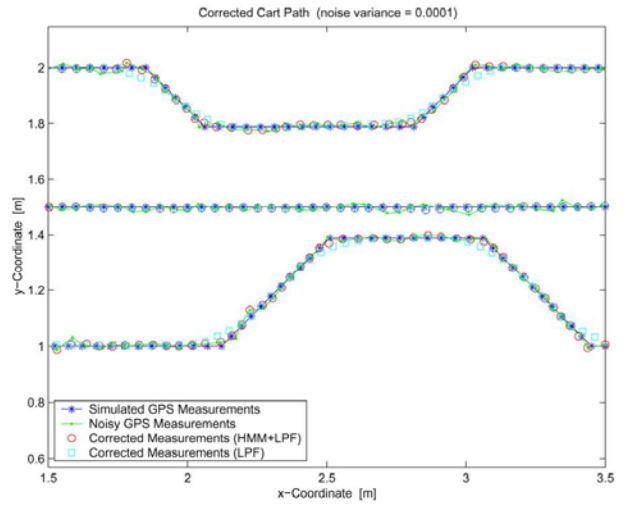
Figure 35: Simulated cart path with noisy GPS measurements and error-corrected GPS measurements for measurement error variance $\sigma^2 = 5 \times 10^{-4}$.



(a) Corrected cart path.

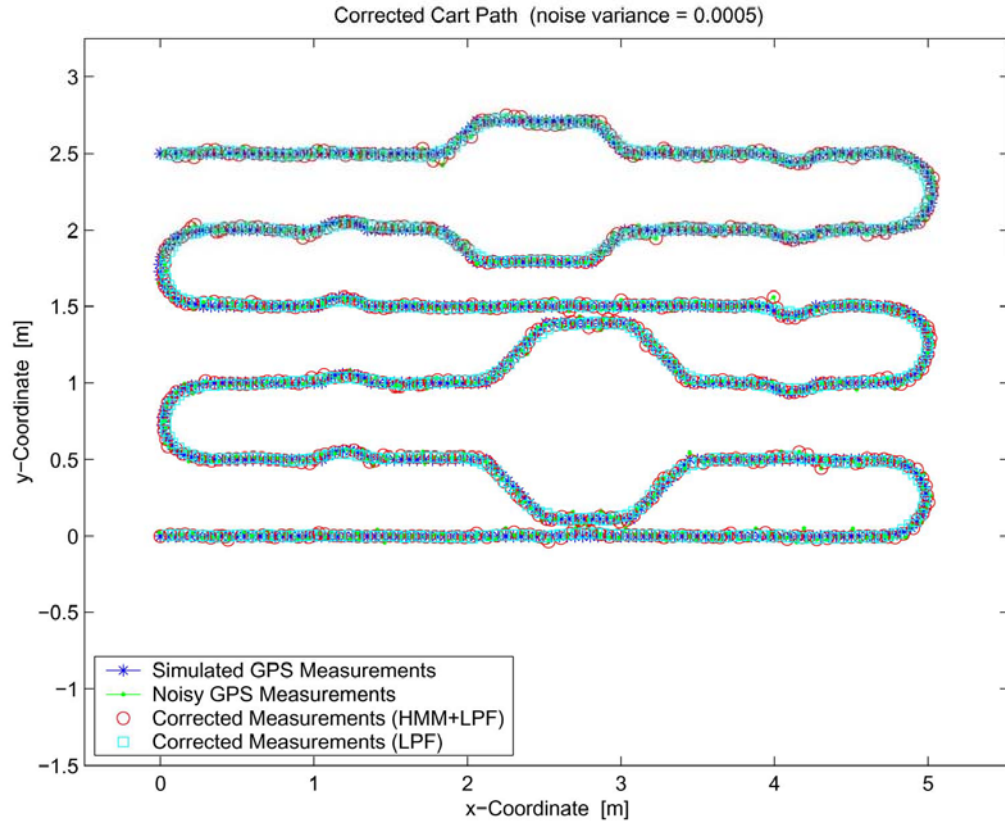


(b) Detail of turn around and cart tilt.

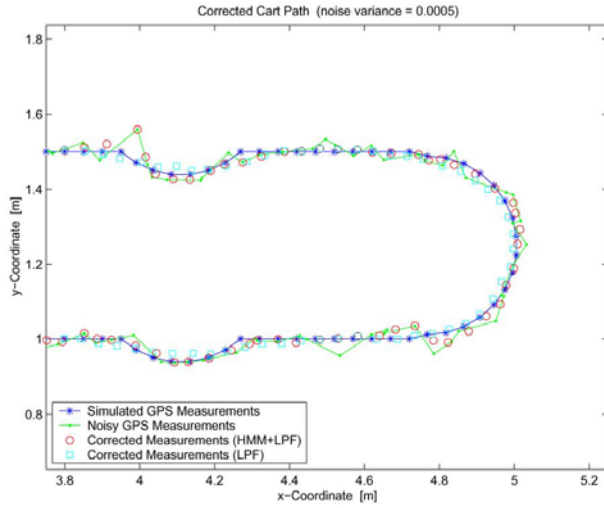


(c) Detail of obstacle avoidance and straight line.

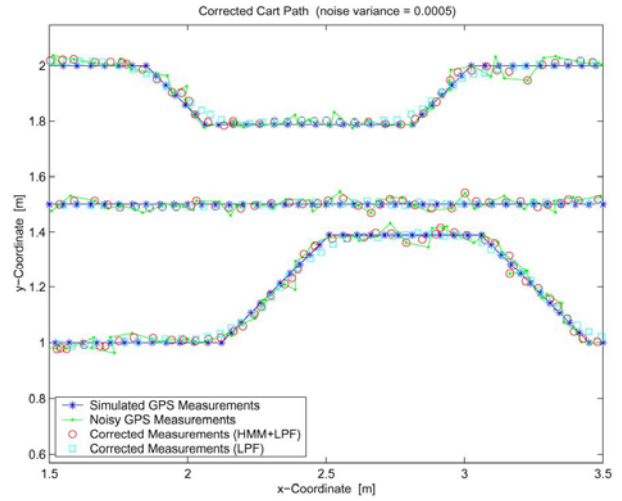
Figure 36: Simulated cart path with noisy GPS measurements and error-corrected GPS measurements for measurement error variance $\sigma^2 = 1 \times 10^{-4}$.



(a) Corrected cart path.

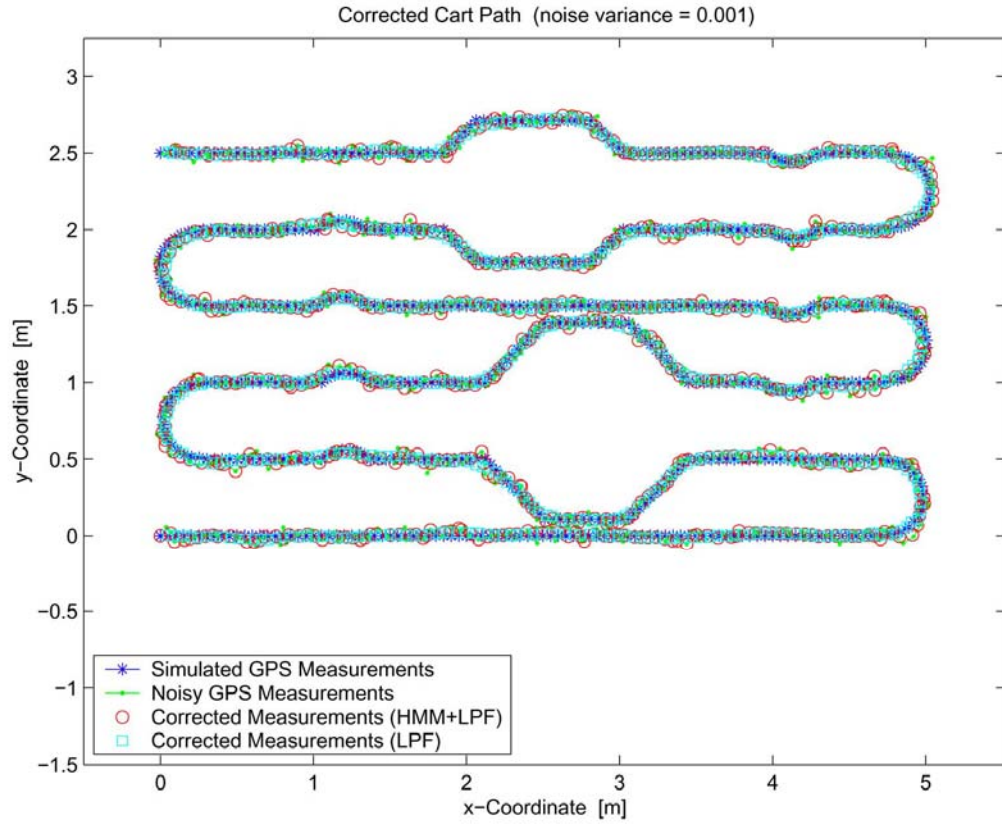


(b) Detail of turn around and cart tilt.

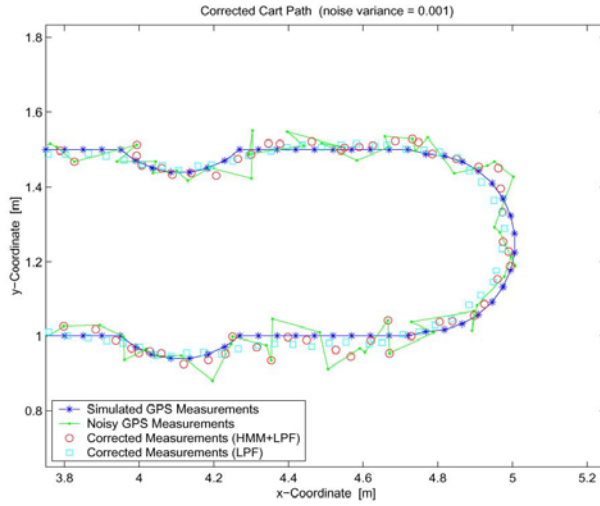


(c) Detail of obstacle avoidance and straight line.

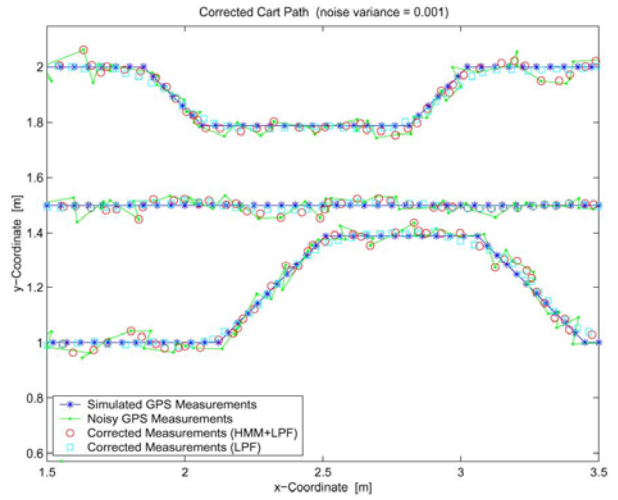
Figure 37: Simulated cart path with noisy GPS measurements and error-corrected GPS measurements for measurement error variance $\sigma^2 = 5 \times 10^{-3}$.



(a) Corrected cart path.



(b) Detail of turn around and cart tilt.



(c) Detail of obstacle avoidance and straight line.

Figure 38: Simulated cart path with noisy GPS measurements and error-corrected GPS measurements for measurement error variance $\sigma^2 = 1 \times 10^{-3}$.

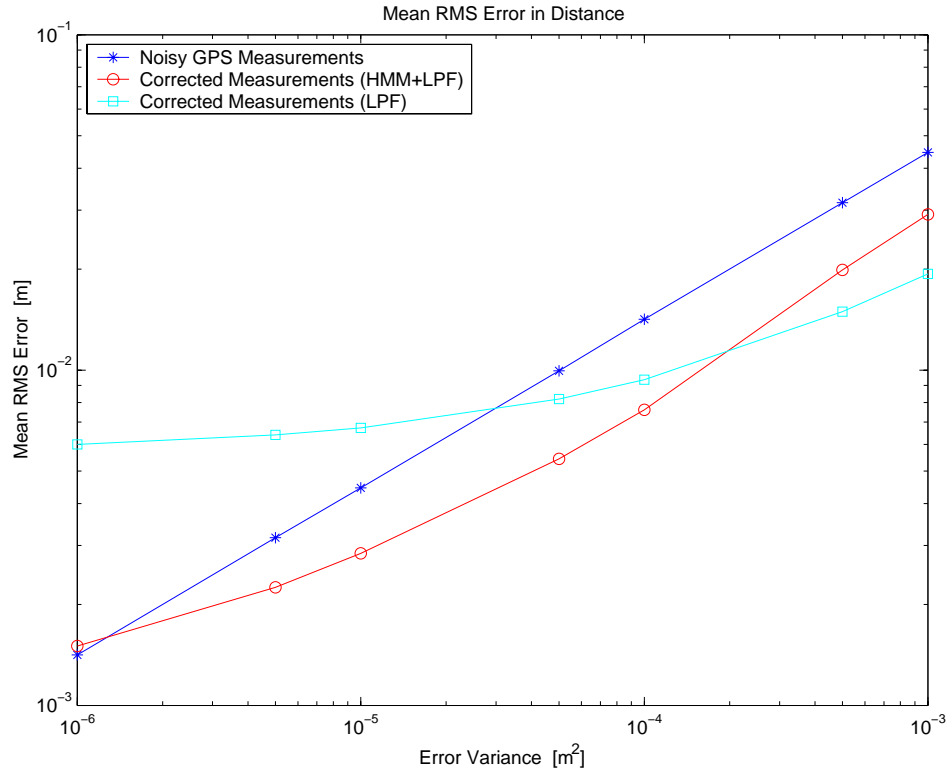


Figure 39: Mean RMS error across all measurements as a function of GPS measurement error variance.

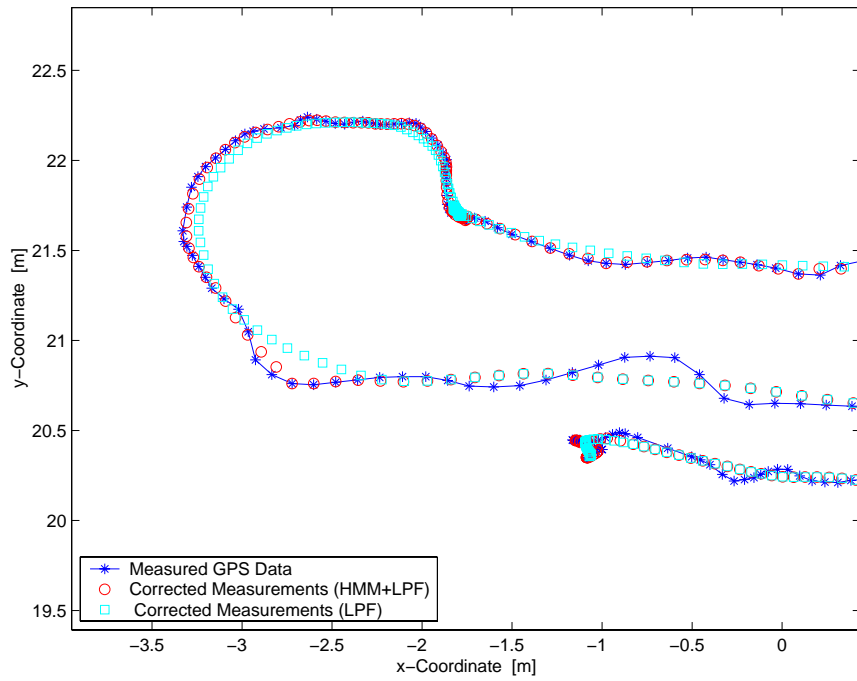


Figure 40: Error correction algorithms applied to data collected at the JPG V demonstration.

6. Three-Dimensional Cart Motion

6.1. Quaternions

When dealing with the cart motion in three dimensions, the common approach is to use a sequence of three Euler angle rotations to completely define the orientation of the cart relative to a reference coordinate system at each point along the cart path. In general, any angle of rotation about a coordinate axis is called an Euler angle. One such sequence that is often used is the yaw(ϕ)–pitch(θ)–roll(ψ) sequence of Figure 41. In describing the evolution of the cart motion, one must keep track of the evolution of the location (x, y, z) and all three Euler angles (ϕ, θ, ψ) .

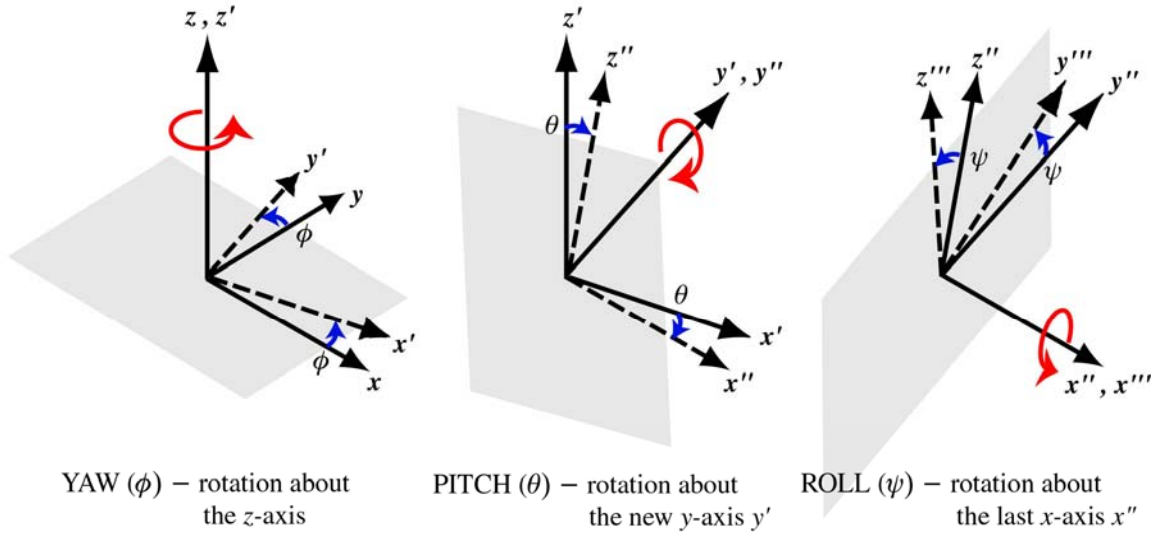


Figure 41: Yaw-Pitch-Roll: A common Euler angle sequence.

If the cart motion were restricted to a plane, the state of each point would be completely defined by its location on the plane (x, y) and the Euler angle ϕ . In this case, a recursive relation for the evolution of ϕ can be written simply as

$$\phi_n = \phi_{n-1} + \Delta\phi_n = \phi_0 + \sum_{i=1}^n \Delta\phi_i \quad , \quad n = 1, 2, 3, \dots$$

where $\Delta\phi_n = \phi_n - \phi_{n-1}$ represents the incremental change in ϕ between points $n-1$ and n , and ϕ_0 represents the initial angle. This same recursive representation for an angle, however, is a natural consequence of multiplying complex numbers (of unit magnitude) in the polar representation. Thus, if we represent the complex number c as

$$c = a + ib = (r \cos \phi) + i(r \sin \phi) \equiv r e^{i\phi} ,$$

where

$$r = |c| = \sqrt{a^2 + b^2} \quad \text{and} \quad \phi = \tan^{-1}\left(\frac{b}{a}\right);$$

then the recursive product of unit complex numbers gives

$$c_n = c_{n-1} \cdot \Delta c_n = c_0 \cdot \prod_{i=1}^n \Delta c_i \equiv e^{i\phi_n} = e^{i\phi_{n-1}} \cdot e^{i\Delta\phi_n} = e^{i\phi_0} \cdot e^{i\left(\sum_{i=1}^n \Delta\phi_i\right)}, \quad n = 1, 2, 3, \dots$$

The above result reinforces the idea that given a point on the unit circle in the complex plane (i.e. c_{n-1} , which represents the angle ϕ_{n-1}), we can multiply it by another unit complex number (i.e. Δc_n) in order to rotate it to a new point on the unit circle (i.e. c_n , which now represents the angle ϕ_n). In other words, points on the unit circle in the complex plane represent all allowable rotations of the cart frame, provided $\theta = \psi = 0$ (i.e. the cart motion is restricted to a plane), and furthermore the evolution of the rotation angle ϕ is completely specified as a path along the unit circle.

If we now relax the condition that the cart motion be restricted to a plane, it turns out that a generalization of the above exists: points on a unit hyper-sphere in four-dimensional complex space represent all allowable rotations in three dimensions, and furthermore the evolution of the rotation Euler angles (ϕ, θ, ψ) is completely specified by a path on the unit hyper-sphere. This is done by extending the above idea for complex numbers, to something called **quaternions** [10-11] – sometimes also called *hyper-complex numbers of rank 4* – where the multiplication operator no longer obeys the commutative law (i.e. the multiplication sequence is important). Thus, if we represent the quaternion q as

$$q = u + \hat{\mathbf{i}}v_1 + \hat{\mathbf{j}}v_2 + \hat{\mathbf{k}}v_3 = u + \mathbf{v},$$

where u is the scalar real part of the quaternion while \mathbf{v} is the vector imaginary part of the quaternion, and the vector components $[v_1, v_2, v_3]$ are mutually orthogonal with the standard directional unit vectors $\hat{\mathbf{i}}, \hat{\mathbf{j}}$ and $\hat{\mathbf{k}}$, respectively; then the unit quaternion can be expressed in a polar-like representation as

$$q = u + \mathbf{v} = \cos \frac{\zeta}{2} + \hat{\mathbf{E}} \sin \frac{\zeta}{2},$$

where $\hat{\mathbf{E}}$ represents a unit vector about which a positive rotation of ζ (as defined by a right-handed coordinate system) takes place. This interpretation stems from the quaternion product of $q \circ \mathbf{r} \circ q^*$, a quantity referred to as *the quaternion rotation operator*, where \mathbf{r} is any three-dimensional vector to be rotated and $q^* = u - \mathbf{v}$ is the complex conjugate of the unit quaternion q . Thus, assuming $\mathbf{r} = \hat{\mathbf{i}}$ and $\hat{\mathbf{E}} = \hat{\mathbf{k}}$, and noting that the quaternion product has the following properties:

$$\hat{\mathbf{i}} \circ \hat{\mathbf{i}} = \hat{\mathbf{j}} \circ \hat{\mathbf{j}} = \hat{\mathbf{k}} \circ \hat{\mathbf{k}} = \hat{\mathbf{i}} \circ \hat{\mathbf{j}} \circ \hat{\mathbf{k}} = -1 ;$$

we have

$$q \circ \mathbf{r} \circ q^* = \hat{\mathbf{i}} \cos \zeta + \hat{\mathbf{j}} \sin \zeta \equiv \mathbf{r}_{rotated} ,$$

where it is clear that the quaternion rotation operator has rotated the vector $\mathbf{r} = \hat{\mathbf{i}}$ by a positive angle ζ about the $\hat{\mathbf{E}} = \hat{\mathbf{k}}$ axis.

Returning to the problem of describing the evolution of the cart motion in three dimensions, we first note that due to a theorem by Euler, *any given sequence of rotations can be represented as a single rotation about a single fixed axis*. The ϕ - θ - ψ sequence can therefore be represented by a single rotation about a single axis, say ζ about $\hat{\mathbf{E}}$, which we have seen can be readily expressed as a unit quaternion q . If we now track from point to point the vector $\hat{\mathbf{E}}$, for example, we have the recursive relation

$$\begin{aligned} \hat{\mathbf{E}}_n &= q_n \circ \hat{\mathbf{E}}_{n-1} \circ q_n^* = q_n \circ (q_{n-1} \circ \hat{\mathbf{E}}_{n-2} \circ q_{n-1}^*) \circ q_n^* = (q_n \circ q_{n-1}) \circ \hat{\mathbf{E}}_{n-2} \circ (q_n \circ q_{n-1})^* \\ &= \left(\prod_{i=1}^n q_i \right) \circ \hat{\mathbf{E}}_0 \circ \left(\prod_{i=1}^n q_i \right)^* , \quad n = 1, 2, 3, \dots \end{aligned}$$

where q_n is the unit quaternion that is needed to rotate the $\hat{\mathbf{E}}_{n-1}$ vector into $\hat{\mathbf{E}}_n$, and

$$\prod_{i=1}^n q_i \equiv q_n \circ q_{n-1} \circ \dots \circ q_1 \circ q_0$$

is itself the unit quaternion needed to rotate the initial vector, $\hat{\mathbf{E}}_0$, into $\hat{\mathbf{E}}_n$. Note that q_0 represents the rotation that takes $\hat{\mathbf{E}}_0$ into $\hat{\mathbf{E}}_1$; q_1 represents the rotation that takes $\hat{\mathbf{E}}_1$ into $\hat{\mathbf{E}}_2$; etc... It is clear, therefore, that the rotational evolution of a vector is efficiently described through a quaternion product of unit quaternions representing incremental rotations at each point along the track, and furthermore that the product outcome is itself a unit quaternion that represents the combined rotation from start to finish.

At this point, it is important to recognize that unit quaternions – which can be thought of as points on a unit hyper-sphere in four dimensions – provide an unambiguous mapping to three-dimensional rotations. For each rotation, however, there exists two corresponding unit quaternions, q and $-q$. Topologically, quaternion space consists of a “double covering”, where q maps to one covering and $-q$ maps to the other. Any continuous quaternion curve on a single covering corresponds to a continuous sequence of rotations [12]. In this case, we can always define a great circle as the unit circle that results from the intersection of the unit sphere in three-dimensional real projective space with a two-dimensional plane containing any two unit quaternions belonging to the curve, as well as the origin of the sphere. There then exists a unique shortest arc along the great circle between the two quaternions, and so the angle that subtends this arc becomes a natural metric to use in order to measure the distance between two unit quaternions. Indeed, if q_0 and q_1 are two unit quaternions, and q_0 rotates to q_1 , then

$$q_1 \equiv (q_1 \circ q_0^*) \circ q_0$$

(since $q_0^* \circ q_0 = u^2 + \mathbf{v} \cdot \mathbf{v} \equiv 1$ for unit quaternions) and the composite quaternion $q_1 \circ q_0^*$ is the rotation connecting them. And since

$$q_1 \circ q_0^* = u_1 u_0 + \mathbf{v}_1 \cdot \mathbf{v}_0 \equiv q_1 \cdot q_0,$$

where $q_1 \cdot q_0$ is the four-dimensional dot product of q_1 and q_0 , this is by definition the cosine of the angular separation between q_0 and q_1 on the unit sphere.

In summary:

- Any three-dimensional rotation can be represented by one of two unit quaternions (q or $-q$).
- All unit quaternions reside on a hyper-sphere in four dimensions. Topologically, they can reside on one of two coverings.
- Any continuous quaternion curve on a single covering corresponds to a continuous sequence of rotations, and has the geometry of three-dimensional real projective space
- The quaternion product of a sequence of points on a curve on the unit sphere is itself another point on the unit sphere, and represents the combined rotation from start to finish for that sequence of points.
- The quaternion product $q_n \circ q_{n-1}^*$ connects point q_{n-1} to q_n on the unit sphere, and represents the cosine of the angular separation between q_{n-1} and q_n on the unit sphere, thus giving the product a geometrical interpretation.

6.2. Advantages of Using Quaternions

It was stated that when dealing with the cart motion in three dimensions, the common approach is to use a sequence of three Euler angle rotations (such as the sequence of Figure 40) to completely define the orientation of the cart relative to a reference coordinate system at each point along the cart path. In this common approach, all rotations are represented by 3 x 3 orthogonal matrices whose determinants are +1 (subsequently to be referred to as *rotation matrices*). The matrix product – also non-commutative – of a sequence of rotation matrices also results in a rotation matrix that represents the combined rotation of the sequence from start to finish. Thus, in an analogous fashion to unit quaternions, a recursive matrix relation expressing the rotational evolution of the cart frame can be formulated. Also analogous to unit quaternions, a matrix product connecting two rotation matrices exists. However, unlike the unit quaternions, a direct geometrical interpretation linking the two matrices does not exist.

There in lies the greatest advantage of using the quaternion formulation over the more common matrix formulation. By knowing the topology and geometry that links a sequence of unit quaternions together, it is possible to manipulate the orientation evolution of the cart frame with

a lot more efficiency and dexterity. The cost, however, is that the new landscape has to be explored and a degree of familiarization attained before this advantage can be exploited.

Take, for example, the interpolation of orientation of the cart body frame given sparse data sampling in the form of the Euler angles ϕ, θ, ψ . In the matrix formulation, there is no straightforward method of finding intermediate rotation matrices given end point rotation matrices. It is not a simple matter of interpolating the Euler angles separately since these angles are obviously correlated. In the quaternion formulation, however, the geometrical interpretation connecting the two unit quaternions allows one to intuitively interpolate between the two points. One simple scheme is the spherical linear interpolation – abbreviated as *slerp* – which linearly interpolates along the great arc connecting the two points and represents a constant speed rotation between the points [13-14]. Many more elaborate schemes also exist [15-16].

By now it should be clear that any filtering (i.e. LPF, linear predictive, etc...) of the orientation data needs to take place in the nonlinear unit quaternion space. Failing to do so will result in non-intuitive methods involving nonlinear transformations, and will therefore be more prone to errors. Using linear approximations might simplify the process, but this then has the potential of resulting in significant deviations from its true behavior if the orientation errors get large.

Another advantage of using quaternions – one that becomes more of an issue when considering real-time processing – is the fact that the only time we need to compute the rotation matrix is when we need to transform to the cart frame. For most other operations, such as the filtering schemes referred to above, we need only look at the quaternions. Since a matrix product requires many more operations than a quaternion product, we can save a lot of time and preserve more numerical accuracy with quaternions than with matrices [17].

6.3. A Quaternion Formulation Using GPS Measurements

This formulation closely follows one suggested by Hanson [18]. His method is applied to the idea of describing the full cart motion – orientation included – using only GPS (x, y, z) measurements. The steps are enumerated below:

1. Create a curve in space which best represents the location of the cart at each point: use GPS data for this. This curve should be described in the tangent-plane reference frame (i.e. earth);
2. At each point along the curve, compute a unit tangent vector $\hat{\mathbf{T}}$. This represents the heading at each point, and will be tied to the x-axis of the cart-body reference frame.
3. If q_i is the quaternion that rotates $\hat{\mathbf{T}}_{i-1}$ to $\hat{\mathbf{T}}_i$, then the recursive relation for the evolution of $\hat{\mathbf{T}}$ is simply

$$\hat{\mathbf{T}}_n = \left(\prod_{i=1}^n q_i \right) \circ \hat{\mathbf{T}}_0 \circ \left(\prod_{i=1}^n q_i \right)^* \quad , \quad n = 1, 2, 3, \dots$$

4. Note, however, that any quaternion $p_i(\xi)$ can replace the quaternion q_i above, provided

$$p_i(\xi) = q_{\hat{\mathbf{T}}_i}(\xi) \circ q_i = (\cos \frac{\xi}{2} + \hat{\mathbf{T}}_i \sin \frac{\xi}{2}) \circ q_i ,$$

since $q_{\hat{\mathbf{T}}_i}(\xi)$ is the quaternion that leaves the direction $\hat{\mathbf{T}}_i$ invariant. The angle ξ serves to parameterize a ring in quaternion space, each point of which corresponds to a particular cart-body frame at (x_i, y_i, z_i) , and all frames are described twice since $0 \leq \xi < 4\pi$. $p_i(\xi)$ is thus known as the *sliding ring constraint*, for obvious reasons.

5. Finally, choose the angle ξ at every cart location by minimizing the quaternion length of the frame assignment for the curve. The justification for this is that there is a unique rotation in the plane of two neighboring tangents that takes each tangent direction to its next neighbor along a curve – this is the geodesic arc connecting the two frames in quaternion space, and is therefore the minimum distance between the quaternion points representing the two frames.

This last step represents a nontrivial step which is highly dependent on the initial orientation chosen for the cart.

7. Summary

The sensitivity of EMI dipole and magnetometer dipole model parameter estimates to errors in the GPS measurements was evaluated through simulations. The results suggest that decreasing the error in the GPS measurements tends to decrease the error in the parameter inversion, with the degree of improvement dependent upon the target parameters and orientation relative to the data collection. This observation motivates the need for techniques to reduce GPS measurement errors. A hidden Markov model for the cart motion has been implemented to broadly characterize the cart motion as linear or nonlinear. The HMM characterizes the cart path so that different error correction techniques can be applied to different segments of the path. For instance, the error correction applied to the linear segments is different from the error correction applied to the nonlinear segments.

Simulations were performed to compare the performance of the HMM followed by segment specific filtering, to the LPF alone. The results show that for low and moderate error levels, where the GPS errors do not impede cart motion characterization, the HMM in general offers better performance. The better performance is due in large part to the improved performance in the regions where the motion is nonlinear. However, for large error variance, where the GPS errors prevent accurate characterization of the cart motion, the LPF alone offers better performance. The same algorithms were then applied to field data collected at the ATD/JPG.

A potential problem for the HMM is in the characterization of perturbations in the cart path due to tilting of the cart. Such segments in the cart path are occasionally mistaken for small detours. To address this deficiency, a quaternion formulation has been proposed as a possible efficient means to track and process the cart orientation as it moves over the uneven terrain. With this added orientation information, ambiguities encountered when attempting to characterize the cart motion as being either linear or nonlinear can be resolved, offering an opportunity for improved robustness for the HMM approach.

8. Directions for Future Research

There are several directions for continued and future research related to this work. One obvious direction is to incorporate the proposed quaternion formulation into the HMM to improve the robustness of the currently implemented approach. This will naturally lead to questions regarding estimates of the initial orientation state and whether an additional sensor, such as an inertial motion unit (IMU), will actually be necessary to make this work. If an IMU is deemed necessary, there is then the question of whether it makes more sense to go with something more sophisticated, such as a Kalman-type filter, to combine the GPS and IMU data. Like the current implementation of the HMM with an LPF of adaptively varying order, the adaptation of the Kalman filter could be guided or influenced by the cart motion characterization determined using the improved HMM.

Another direction, which will be site dependent, might be to closely examine the relationship between the characteristics of the ground surface and the distributions of GPS errors. The relationship between the ground surface and GPS error distributions could then be utilized to guide the design of the HMM for the cart motion model.

9. References

- [1]. Bell, T., B. Barrow, and J.T. Miller (2001), "Subsurface Discrimination Using Electromagnetic Induction Sensors," *IEEE Trans. Geosci. Remote Sensing*, vol. 39, pp. 1286-1293.
- [2]. Pasion, L. R. and D. W. Oldenburg (2001), "A Discrimination Algorithm for UXO Using Time Domain Electromagnetics," *Journal of Engineering and Environmental Geophysics*, 6, no.2, pp. 91-102.
- [3]. Norton, S. and I. J. Won (2001), "Identification of Buried Unexploded Ordnance From Broadband Electromagnetic Induction Data," *IEEE Trans. Geosci. Remote Sensing*, vol. 39, no. 10, pp. 2253-2261.
- [4]. Khadr, N., B. J. Barrow, and T. H. Bell (1998), "Target Shape Classification Using Electromagnetic Induction Sensor Data," *Proceedings of UXO Forum '98*.
- [5]. "UXO technology demonstration program at Jefferson Proving Ground Phase IV," Tech. Rep. SFIM-AEC-ET-CR-99 051, U.S. Army Environ. Center, Naval Explosive Ordnance Disposal Tech. Div., May 1999.
- [6]. Barrow, B. and H. H. Nelson (2001), "Effects of Positioning Error on Inverting EMI Data for UXO Discrimination Using the MTADS Platform," *The UXO/Countermine Forum Conference Proceedings*, New Orleans, LA.

- [7]. Collins, L. M., Y. Zhang, J. Li, L. Carin, S. Hart, S. Rose-Pehrsson, H. Nelson, and J. McDonald (2001) “A comparison of the performance of statistical and fuzzy algorithms for unexploded ordnance detection.” *IEEE Transactions on Fuzzy Systems*, 9(1):17–30.
- [8]. Stark, H. and J. W. Woods (2002) *Probability and Random Variables with Applications to Signal Processing*. Prentice-Hall, Upper Saddle River, NJ, 3rd edition.
- [9]. Forney, Jr., G. D. (1973) “The Viterbi Algorithm.” *Proceedings of the IEEE*, 61(3):268–278.
- [10]. Hamilton, W. R. (1847) “On Quaternions.” *Proceedings of the Royal Irish Academy*, 3, pp. 1-16.
- [11]. Kuipers, J. (1999) *Quaternions and Rotation Sequences*. Princeton University Press.
- [12]. Shoemake, K. (1985) “Animating rotation with quaternion curves.” *Computer Graphics (SIGGRAPH '85 Proceedings)*, vol. 19, pp. 245–254.
- [13]. Pletincks, D. (1989) “Quaternion calculus as a basic tool in computer graphics.” *The Visual Computer* 5, 1, 2–13.
- [14]. Barr, A. H., B. Currin, S. Gabriel, and J. F. Hughes (1992) “Smooth interpolation of orientations with angular velocity constraints using quaternions.” *Computer Graphics (SIGGRAPH '92 Proceedings)*, vol. 26, pp. 313–320.
- [15]. Johnstone, J. and J. Williams. (1995) “Rational control of orientation for animation.” *Proceedings of Graphics Interface '95*, pages 179–186.
- [16]. Nielson, G. M. (1993) *Models and Techniques in Computer Animation*, (Magenat Thalmann N and Thalmann D, eds), Springer-Verlag, Tokyo, pp.75-93.
- [17]. Salamin, E. (1979) “Applications of Quaternions to Computation with Rotations.” Working Paper, Stanford AI Lab.
- [18]. Hanson, A. J. (1998) “Constrained optimal framings of curves and surfaces using quaternion gauss maps.” *Proceedings of Visualization '98*, IEEE Computer Society Press, pp. 375–382. Missing pages 2 and 4 in original Proceedings; correct version in second printing of Proceedings, on conference CDROM, or <http://ftp.cs.indiana.edu/pub/hanson/Vis98/vis98.quat.pdf>.

10. Technical Publications

“Correcting GPS Measurement Errors Induced by System Motion over Uneven Terrain,” Stacy L. Tatum, Leslie M. Collins, Nagi Khadr and Bruce J. Barrow, *Proceedings of SPIE* Vol.

#5089, *Detection and Remediation Technologies for Mines and Minelike Targets VIII* (Conference 5089), Orlando, FL, April, 2003.